JGR Atmospheres

RESEARCH ARTICLE
10.1029/2020JD032653

Special Section:
Bridging Weather and Climate: Subseasonal-to-Seasonal (S2S) Prediction

The Global Teleconnection Signature of the Madden-Julian Oscillation and Its Modulation by the Quasi-Biennial Oscillation

Benjamin A. Toms[1], **Elizabeth A. Barnes**[1], **Eric D. Maloney**[1], **and Susan C. van den Heever**[1]

[1]Department of Atmospheric Science, Colorado State University, Fort Collins, CO, USA

Abstract Recent research has suggested that the tropical and extratropical character of the Madden-Julian oscillation (MJO) depends on the state of the stratospheric quasi-biennial oscillation (QBO). With this in mind, we use both reanalysis and a global climate model (CESM2-WACCM) to analyze the global character of upper tropospheric-lower stratospheric geopotential height anomalies connected with the MJO and quantify dependencies of these teleconnections on the state of the QBO. We find that the global teleconnection signature of the MJO depends upon the state of the QBO. Globally, within reanalysis the fraction of 20- to 90-day 250-hPa geopotential height variance linked to the MJO is largest during boreal winter and summer for easterly QBO phases and smallest during westerly QBO phases of boreal winter. The difference between QBO phases is mostly driven by changes in the tropical signature of the MJO, although during boreal winter the Northern Hemispheric teleconnections are particularly more prominent during easterly QBO phases. Otherwise, the QBO modulation of extratropical MJO teleconnections is mainly realized through changes in the locations of the teleconnections. A QBO-MJO relationship is also apparent within CESM2-WACCM but is weaker than that observed. This extratropical modulation implies that the regions that benefit from increased subseasonal predictability due to the MJO may also change as a function of the QBO. In a broader sense, these findings emphasize that knowledge of the tropical stratospheric state, particularly as it relates to the QBO, is important for understanding the connections between the MJO and the extratropics.

Key Points:
- The QBO modulates the locations of MJO teleconnections, mainly through the locations in which they occur
- The modulation is greatest during boreal winter but occurs to some extent during all seasons
- A modulation also exists within CESM2-WACCM but is weaker and has a different spatial pattern

Supporting Information:
- Supporting Information S1

Correspondence to:
B. A. Toms,
ben.toms@colostate.edu

Citation:
Toms, B., A, Barnes, E. A., Maloney, E. D., & van den Heever, S. C. (2020). The global teleconnection signature of the Madden-Julian oscillation and its modulation by the quasi-biennial oscillation. *Journal of Geophysical Research: Atmospheres*, *125*, e2020JD032653. https://doi.org/10.1029/2020JD032653

Received 21 FEB 2020
Accepted 29 FEB 2020
Accepted article online 4 MAR 2020

Author Contributions
Conceptualization: Benjamin A. Toms, Elizabeth A. Barnes, Eric D. Maloney
Data curation: Benjamin A. Toms, Elizabeth A. Barnes, Eric D. Maloney, Susan C. van den Heever
Funding Acquisition: Benjamin A. Toms, Elizabeth A. Barnes, Eric D. Maloney, Susan C. van den Heever
Methodology: Benjamin A. Toms, Elizabeth A. Barnes, Eric D. Maloney
Software: Benjamin A. Toms
Validation: Benjamin A. Toms
Writing - Original Draft: Benjamin A. Toms

1. Introduction

While mainly defined as a tropical disturbance, the Madden-Julian oscillation (MJO Madden & Julian, 1971, 1972, 1994; Zhang, 2005) impacts the global atmosphere through teleconnections. Its tropical form is manifested in part through a convective anomaly that originates within the tropical western Indian Ocean and propagates across the Indo-Pacific warm pool and into the Central Pacific (Hendon & Liebmann, 1994; Kemball-Cook & Weare, 2001; Powell & Houze, 2013). The convective anomaly interacts with and excites other atmospheric waves across a broad range of scales, including equatorially circumnavigating Kelvin waves (Haertel et al., 2015; Powell, 2017) and mixed Rossby gravity waves (Bessafi & Wheeler, 2006). Rossby gyres flank its convective response, extending into the subtropics (Kiladis et al., 2005). Rossby waves also emanate poleward from the convective anomaly within the Indo-Pacific warm pool, generating a Rossby wave train across the northern Pacific and into North America (Henderson et al., 2016; Seo & Lee, 2017; Tseng et al., 2019). Additional midlatitude linkages have been documented in the Southern Hemisphere, wherein the rainfall of Australia, subtropical South America, and Africa can be modulated by the MJO (Alvarez et al., 2017; Pohl et al., 2007; Wheeler et al., 2009).

The quasi-biennial oscillation (QBO) is another periodic tropical phenomenon and takes the form of an oscillation in zonal wind anomalies within the tropical stratosphere that completes a cycle approximately every 28 months (Baldwin et al., 2001). The QBO is driven by the deposition of easterly and westerly momentum into the stratosphere by an amalgamation of tropical waves ranging from convectively generated internal gravity waves on the scale of tens to hundreds of kilometers to Kelvin waves with scales of thousands of kilometers (Kawatani et al., 2010; Lindzen & Holton, 1968). The QBO modulates the vertical propagation of planetary scale waves (Yang et al., 2012), which can also modulate the development of the lower

Formal Analysis: Benjamin A. Toms, Elizabeth A. Barnes, Eric D. Maloney
Investigation: Benjamin A. Toms, Elizabeth A. Barnes, Eric D. Maloney
Resources: Benjamin A. Toms, Susan C. van den Heever
Supervision: Elizabeth A. Barnes, Susan C. van den Heever
Visualization: Benjamin A. Toms
Writing - review & editing: Benjamin A. Toms, Elizabeth A. Barnes, Eric D. Maloney, Susan C. van den Heever

stratospheric polar vortex (Baldwin & Dunkerton, 1998), and further cascades into a range of tropospheric extratropical responses (Boer & Hamilton, 2008; Folland et al., 2012; Thompson et al., 2002). The global influences of the QBO have been investigated over the past decades, and recent research suggests that both the tropical and extratropical responses to the MJO may depend upon the state of the QBO.

For example, the seasonal average amplitude of the tropical top-of-atmosphere longwave radiative response to the MJO is approximately doubled during easterly QBO phases relative to westerly QBO phases during boreal winter (Son et al., 2017). This increase in boreal winter MJO activity during easterly QBO phases is possibly caused by either a greater number and increased longevity of MJO events (Zhang & Zhang, 2018) or stronger MJO events with greater duration (Hendon & Abhik, 2018). Easterly QBO phases favor a more active MJO over the Maritime Continent than westerly QBO phases (Densmore et al., 2019), which may explain the propagation of the MJO further into the east Pacific. Easterly QBO phases also induce anomalously cold temperature at the tropical tropopause, which could encourage more vigorous convection and thereby a healthier MJO (Martin et al., 2019). Furthermore, connections between the MJO and the North Pacific storm track are modulated by the QBO, with easterly QBO phases favoring a more longitudinally expansive and intense storm track (Wang et al., 2018). Other studies have shown that the predictability of the MJO and its teleconnections depends on the phase of the QBO (Lim et al., 2019; Mayer & Barnes, 2019; Mundhenk et al., 2018). While these linkages between the MJO and QBO have been discovered, the mechanisms behind the relationships is still relatively unclear, although it has been hypothesized that they are related to temperature and static stability anomalies within the upper troposphere associated with the QBO (Densmore et al., 2019; Klotzbach et al., 2019; Martin et al., 2019).

However, it is still unclear to what extent the QBO modulates the global teleconnection signature of the MJO. An understanding of how the QBO modulates such MJO teleconnections would benefit efforts to improve prediction on subseasonal timescales within the extratropics, such as those related to extreme weather patterns (e.g., Baggett et al., 2018; Matsueda & Takaya, 2015; Mundhenk et al., 2018). The goal of this research is therefore to determine when and where the QBO modulates the global teleconnection signature of the MJO, and if so, to what extent. In order to do so, we use cross-spectral analysis to quantify the dependence of the relationship between the MJO and 250-hPa geopotential height variability across the globe on QBO phase. Specifically, we use both global reanalysis and a fully coupled global climate model (GCM), to quantify this relationship. We first detail the indices we use to define the MJO within both the observational record and the GCM, and then we discuss the specific methods used to quantify the relationship between the global signature of the MJO and the QBO. The dependence of the global signature of the MJO on the QBO is then detailed, first as it appears within reanalysis and then as it appears within the GCM.

2. Data and Methods

2.1. Reanalysis and Global Circulation Model

We use ERA-Interim reanalysis (Dee et al., 2011), which is a reanalysis product from the European Center for Medium-Range Weather Forecasts (ECMWF). ERA-Interim has been used extensively for MJO-related analyses and has been shown to accurately reproduce both the tropical structure of the MJO and its impacts on the extratropics (e.g., Dee et al., 2011; DeMott et al., 2013; Jiang et al., 2011). We use daily ERA-Interim output from 1 January 1980 through 31 December 2016 with a grid spacing of 0.75° by 0.75°.

For the climate model, we use output from the Whole Atmosphere Community Climate Model (WACCM Liu et al., 2018) version of the Community Earth System Model Version 2 (CESM2, hereafter CESM2-WACCM Lauritzen et al., 2018) available through the Coupled Model Intercomparison Project Phase 6 (CMIP6 Eyring et al., 2016) archive. We use daily output from the three historical CESM2-WACCM CMIP6 simulations which span from 1 January 1850 through 31 December 2014, with a grid spacing of approximately 1° by 1.25°. WACCM is a high-top chemistry coupled climate model that extends to 6×10^{-6} hPa and contains an internally generated representation of the QBO. It is important for GCMs to have a sufficiently resolved stratosphere to produce a robust QBO (Charlton-Perez et al., 2013), which is not offered by most low-top CMIP6 simulations that extend only into the lower stratosphere. CESM2-WACCM has been shown to accurately model sudden-stratospheric warming events (Liu et al., 2019), and similar model configurations within CESM1-WACCM have been shown to produce a QBO representative of observations (Richter et al., 2020), which lends confidence that CESM2-WACCM is capable of simulating an accurate QBO, as well.

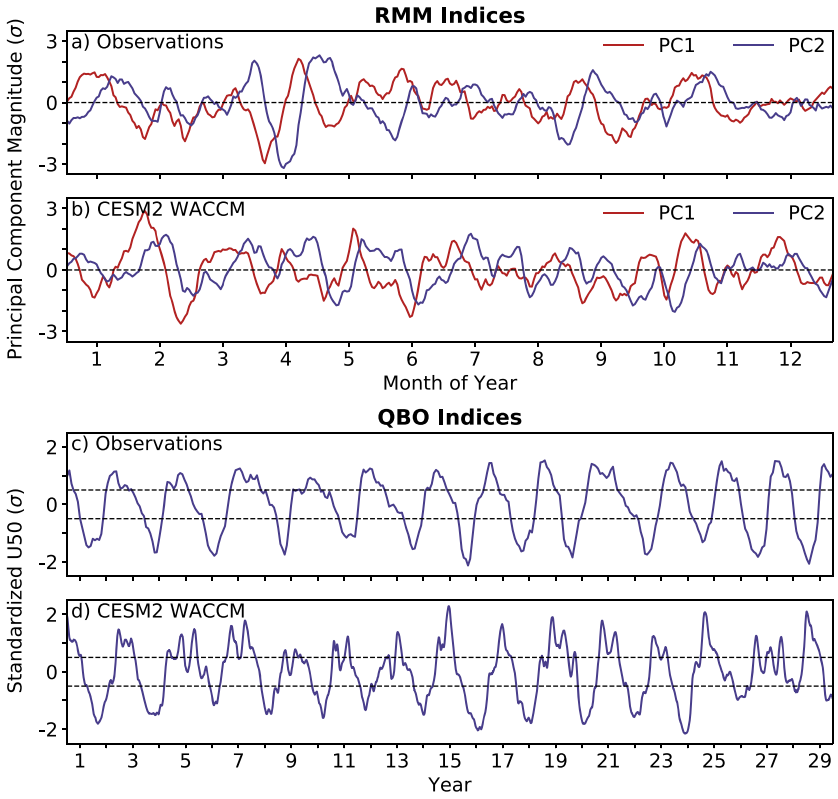

Figure 1. Comparisons of the (a, b) daily observational and CESM2-WACCM RMM principal component time series and (c, d) monthly observational and CESM2-WACCM QBO time series. Note that the *x*-axis scales are different between (a, b) and (c, d). Within (c, d) the dashed black lines denote the positive and negative 0.5σ values, above and below which we define as a significant QBO anomaly.

It is uncommon for climate models to adequately simulate both an MJO and QBO, and CESM2-WACCM therefore presents a unique opportunity to test the capability of such a model to capture the relationship between the MJO and QBO, should a relationship exist within the observational record. Furthermore, if a model such as CESM2-WACCM can accurately simulate any observed relationships between the MJO and QBO, then they may be useful tools for elucidating physical mechanisms driving such a relationship. For this particular analysis, CESM2-WACCM enables the usage of many more samples than the observational data record contains: The CESM2-WACCM CMIP6 simulations collectively offer 495 years of information, whereas reanalysis offers approximately 40 years.

2.2. Definition of the MJO, QBO, and Teleconnections

2.2.1. The MJO and the QBO

We use the Realtime Multivariate MJO (RMM) index (Wheeler & Hendon, 2004) to define the state of the MJO given its simplicity and therefore reproducibility within GCM output. RMM is based on principal component analysis of the combination of tropical outgoing longwave radiation (OLR), 850-hPa zonal wind, and 200-hPa zonal wind fields and captures both the convective and circulation patterns associated with the MJO. For the observational record, the RMM index was downloaded from the Australian Bureau of Meteorology (http://www.bom.gov.au/climate/mjo/), while for CESM2-WACCM the index is computed using the model output. We use 250-hPa zonal winds in the calculation of the RMM index for CESM2-WACCM since daily 200-hPa output is not available for CESM2-WACCM through the CMIP6 archive. The process by which RMM is calculated for CESM2-WACCM is detailed in the supporting information. The oscillatory pattern of the RMM principal components derived from CESM2-WACCM is similar to that of the observational RMM (Figures 1a and 1b). In addition, the evolution of OLR, 850-hPa zonal wind, and 250-hPa zonal wind throughout the lifecycle of the MJO within CESM2-WACCM is similar to the observed MJO (Figure 2). The most prominent differences occur over the Maritime Continent (longitudes of 100° to 150°), where the simulated MJO temporarily stalls while the observed MJO continuously accelerates eastward. Lagged

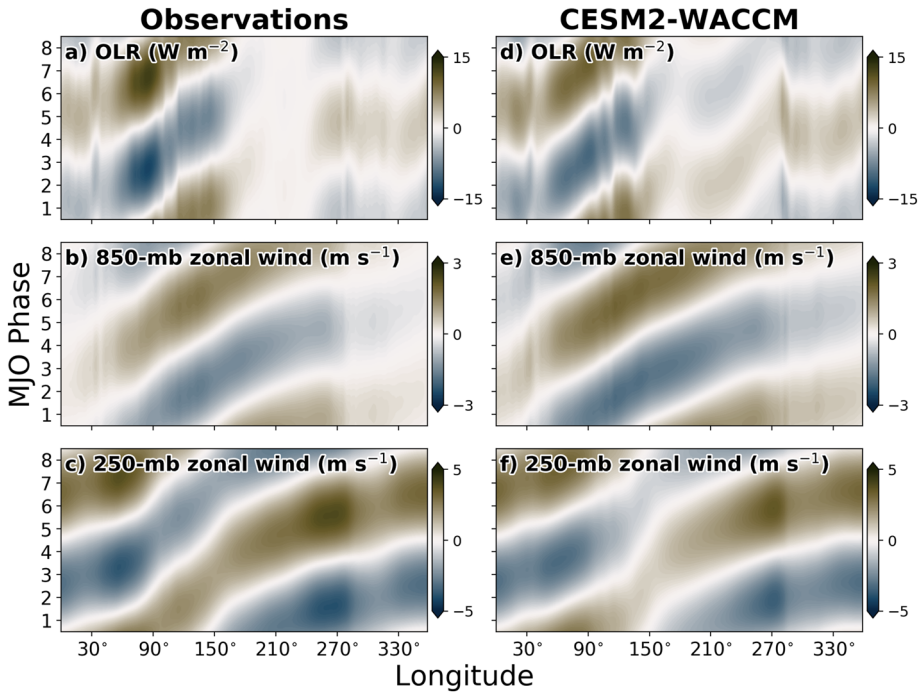

Figure 2. Comparisons of the equatorial structure of the MJO within ERA-Interim and CESM2-WACCM in OLR (a, d), 850-hPa zonal wind (b, e), and 250-hPa zonal wind (c, f). The phase of the MJO is plotted on the *y*-axis, and longitude is plotted along the *x*-axis. The plotted values represent the anomalies associated with an MJO event with a magnitude of one standard deviation throughout its entire phase space. To generate these anomalies, the principal components for the observational and CESM2-WACCM RMM indices were regressed onto the equatorially averaged anomalous fields of OLR, 850-hPa zonal wind, and 200-hPa zonal wind, separately. The calculation procedure for the equatorially averaged anomalous fields is detailed in the supporting information.

correlations of the RMM time series clearly depict a propagating MJO within CESM2-WACCM, albeit with a slower eastward progression than within observations (supporting information Figure S4).

Zonal wind anomalies associated with the QBO are most pronounced within the lower to middle equatorial stratosphere, generally spanning from approximately 70 to 10 hPa (Naujokat, 1986). The state of the QBO is commonly defined according to 30- or 50-hPa zonal wind anomalies since these pressure levels capture the core of the QBO (Holton & Tan, 1980; Pascoe et al., 2005), and so we define the QBO based on 50-hPa zonal wind anomalies. The observational index for the QBO was downloaded from NCEP (https://www.cpc.ncep.noaa.gov/data/indices/qbo.u50.index) and represents the standardized equatorial 50-hPa zonal wind anomalies from 1 January 1980 through 31 December 2016. The QBO index for CESM2-WACCM is also defined as the standardized equatorial 50-hPa zonal wind anomaly and is calculated from the mean and standard deviation across all three historical CESM2-WACCM CMIP6 simulations. The CESM2-WACCM QBO exhibits similar characteristics to the observed QBO, at least at 50 hPa, although there are some differences (Figures 1c and 1d). For example, the oscillatory period for the simulated QBO (~24 months) is slightly shorter than the observed QBO (~28 months). There are also higher frequency modes of variability within the simulated QBO, particularly during the positive phases. Overall, however, it appears that CESM2-WACCM does generate a QBO with characteristics that are generally similar to the observed QBO, at least at 50 hPa.

It is worth noting that the configuration of CESM2-WACCM used in the CMIP6 archive insufficiently represents the QBO within the lower stratosphere, which may have implications for interactions between the troposphere and stratosphere and therefore the modeled relationship between the MJO and QBO. Figure 3 shows stratospheric zonal wind anomalies within ERA-Interim and CESM2-WACCM, both in raw form and standardized on a level-by-level basis. The raw zonal wind anomalies show that the QBO within CESM2-WACCM does not descend completely to the tropopause. However, when the zonal wind anomalies are standardized with respect to the mean and standard deviation of each respective level in the model, it is apparent that the influence of the QBO does extend to the tropopause. The QBO within CESM2-WACCM

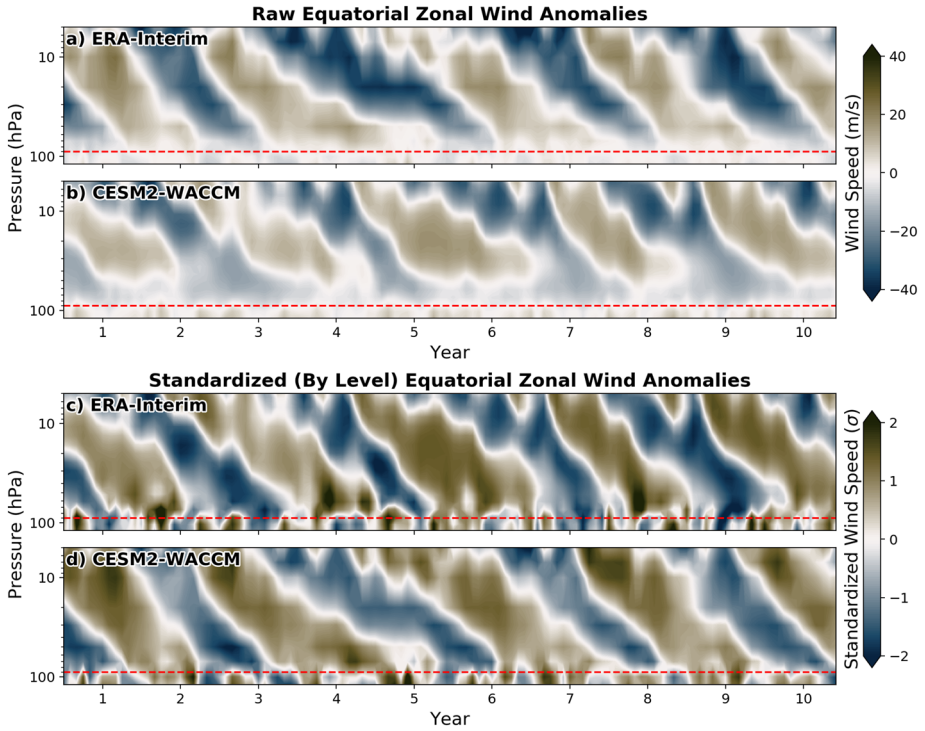

Figure 3. Comparisons of the stratospheric zonal wind within ERA-Interim and CESM2-WACCM. Raw equatorial zonal wind anomalies are shown in (a) and (b), while (c) and (d) show the zonal wind anomalies after they are standardized for each vertical model level separately.

is therefore mainly realized at the tropopause as a slowing of the otherwise predominant easterly flow, with occasional reversals toward westerly flow. This deficiency suggests that the CMIP6 configuration of CESM2-WACCM may not be able to fully capture the interactions between the MJO and QBO should it depend on an oscillatory reversal of the stratospheric zonal wind at the tropopause.

Except for the QBO-ignorant analyses which include all years regardless of QBO amplitude, only seasons during which the average magnitude of zonal wind anomalies at 50 hPa is greater than 0.5σ (σ = 7.27 m s^{-1} for observations and 5.76 m s^{-1} for CESM2-WACCM) are considered to ensure that the QBO signal is strong. Additionally, the four meteorological seasons are considered separately, divided into December/January/February (DJF), March/April/May (MAM), June/July/August (JJA), and September/October/November (SON) as boreal winter, spring, summer, and fall, respectively. Each season is defined as a 90-day period starting from the first day of the first month of the season. Figure 4 presents all such seasons that satisfy the QBO-magnitude criterion for the observational record. For CESM2-WACCM, the minimum number of samples for the various combinations of seasons and QBO phases is 138 for boreal spring of westerly QBO phases, with a maximum of 234 samples during boreal summer of westerly QBO phases.

2.2.2. MJO Teleconnections

We use anomalies in 250-hPa geopotential height to identify the global teleconnection signature of the MJO, although the conclusions are consistent across the 500- through 200-hPa pressure range (not shown). The consistency across this pressure range is supported by previous research which has found that global teleconnections associated with the MJO are similarly apparent within geopotential height anomalies at pressure levels ranging from 500 to 200 hPa (Alvarez et al., 2017; Henderson & Maloney, 2018; Henderson et al., 2016; Riddle et al., 2013). Anomalies in 250-hPa geopotential height are calculated independently for each grid point by subtracting the record-length mean, linear trend, and seasonal cycle for each respective grid point. We define the seasonal cycle for each grid point as the first three harmonics of the mean daily annual cycle throughout the record period, which is 1980 through 2016 for reanalysis and the entire duration of the simulations for CESM2-WACCM (1850 through 2014). The prevalence of MJO teleconnections is then quantified via the magnitude-squared coherence between time series of 250-hPa geopotential height anomalies at each grid box within the reanalysis and the two RMM principal components, divided into season and QBO phase.

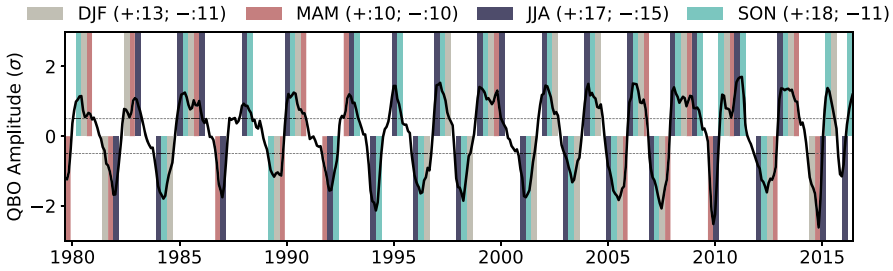

Figure 4. Standardized 50-hPa zonal wind anomalies for 1 January 1980 through 31 December 2016. Seasons wherein the average QBO magnitude is greater than 0.5 standard deviations are highlighted, with seasons of significant QBO anomalies that coincide with significant ENSO anomalies (ONI > 1 °C) shaded gray. The total number of seasons during which significant QBO anomalies occur without significant ENSO anomalies is tallied within the legend above the figure
(W for westerly QBO and E for easterly QBO), with the number of all seasons regardless of ENSO phase tallied in parantheses. Seasons during which the ENSO anomalies are significant are discarded from the westerly and easterly QBO analyses, although the results in which all samples are included regardless of ENSO amplitude are included within the supporting information.

Of note, the El Niño-Southern Oscillation (ENSO; e.g., Ashok et al., 2007; Diaz et al., 2001; Trenberth, 1997; Yu & Kim, 2013) also occurs on interannual timescales (~3 to 8 years) and has been shown to occasionally be modulated by the MJO (Slingo et al., 1999; Zhang & Gottschalck, 2002) and modulate both the tropical structure and extratropical teleconnections of the MJO (Henderson & Maloney, 2018; Kessler, 2001; Moon et al., 2011; Roundy et al., 2010; Takahashi & Shirooka, 2014). ENSO is therefore a potential source of uncertainty in the causality of the relationships between the MJO and the QBO. As is discussed in the subsequent section, we consider only the relationship between the MJO and 250-hPa geopotential height, and so ENSO teleconnections themselves are not included within our analysis. Rather, any impacts of ENSO would be realized through a modulation of the MJO itself and its teleconnections. We have found, however, that the removal of ENSO from the analysis does not change our conclusions, and we therefore do not remove periods with strong ENSO events. Further discussion is available in the supporting information.

2.3. Application of Magnitude-Squared Coherence to Teleconnections of the MJO

We isolate the global signature of the MJO using magnitude-squared coherence (Coh^2), the details of which are presented within the appendix. Coh^2 has been used for previous research on the MJO, to quantify the relationships between MJO index principal components, tropospheric temperature and OLR in the context of the MJO, and tropospheric zonal wind and OLR, in addition the original work of Madden and Julian (1971) and many other examples (see, e.g., Adames et al., 2017; Madden & Julian, 1971; Sakaeda et al., 2017; Wheeler & Hendon, 2004). Coh^2 is typically calculated from an average of cross spectra from multiple samples of two time series and can thereby be thought of as a metric for the consistency of the amplitude and phase relationships between two time series, x and y, across numerous samples. Coh^2 ranges from 0 to 1 for each Fourier mode, k, of the time series, where 0 corresponds to the case where no magnitude or phase relationships exist at wave number k and 1 corresponds to the case where the amplitude and phase relationships between x and y are identical at wave number k across all samples. Coh^2 can be separated into its Fourier modes, which allows for the interpretation of relationships between two time series for specific frequency bands. Most important for this study, Coh^2 can be interpreted as the fraction of signal y that can be explained by variability in signal x at a particular frequency or across a frequency band. Furthermore, since Coh^2 is calculated across multiple samples and is an estimate of the similarities in the relationship between x and y across each sample, it is a metric for the *coherence* of the relationship between two signals rather than the magnitude. Throughout the remainder of this paper, we will therefore refer to the Coh^2 between two time series as an estimate of the coherence of their magnitude and phase relationships.

The subsequent analyses consider Coh^2 averaged over the 20- to 90-day band, since this is a representative timescale of the MJO (Wheeler & Hendon, 2004). Since we define each season as a 90-day period, the analyses consider atmospheric variability with periods of up to 90 days and therefore consider the intraseasonal influences of the MJO. We quantify the periodic relationship between the MJO and 250-hPa geopotential height anomalies according to the following procedure, which is completed for every grid cell at 250 hPa

within both ERA-Interm and CESM2-WACCM and separately for the two principal components of the observational and CESM2-WACCM RMM indices. First, the Coh^2 is calculated between the time series of the principal component and 250-hPa geopotential height, separately for each season and QBO phase, where the samples for the Coh^2 calculation are the separate seasons within each QBO phase, as listed in Figure 4. The Coh^2 is then averaged across the 20- to 90-day band, which results in a 20- to 90-day mean Coh^2 between the principal component of RMM and 250-hPa geopotential height.

We estimate the fraction of intraseasonal variance in 250-hPa geopotential height that is linked to the MJO at every location across the globe. To do so, the power spectra for 250-hPa geopotential height are calculated at each grid cell separately for each QBO phase and season and then normalized by the integrated power across all harmonic modes in the 20- to 90-day band. Then, the Coh^2 between the RMM principal component and 250-hPa geopotential height is multiplied by the normalized power spectra for each Fourier mode individually to calculate the fraction of variance in each Fourier mode explained by the MJO. This quantity is then summed across the 20- to 90-day band. This process is conceptually similar to estimating the fraction of variance in 250-hPa geopotential height associated with the MJO by multiplying the variance in 250-hPa geopotential height by the squared correlation between RMM and 250-hPa geopotential height. Although as previously discussed, we use Coh^2 since it can better capture the covariance between two periodic signals convoluted by superimposed waves (see appendix for additional discussion).

Two separate techniques are used to estimate the Coh^2 for the reanalysis and CESM2-WACCM because of the drastically different sample sizes. For the reanalysis, 5 years are selected from the total available years for each season and QBO phase for a total of 250 subsamples, and the mean Coh^2 across all 250 subsamples is presented. This process is completed separately for each season and QBO phase. For CESM2-WACCM, we simply calculate the Coh^2 for 138 randomly selected samples for all seasons and QBO phases. We use 138 randomly selected samples because this is the number of boreal spring seasons that occur during westerly QBO phases, and so we use the same number of samples for all seasons and QBO phases. A detailed discussion of why we use these two separate methods is within the appendix.

It is worth mentioning that PC1 and PC2 of RMM do not necessarily contain the same information about the MJO, since the MJO very rarely completes an oscillation through its phase space while maintaining a constant amplitude. In fact, the Coh^2 between PC1 and PC2 of RMM is 0.685 for the observational record and 0.724 for the RMM index derived from CESM2-WACCM. This implies, for example, that 31.5% of the information carried within each RMM principal component time series is unique from the other for the observational record. However, it is difficult to determine whether this unique information is caused by intraseasonal variability extraneous to the MJO that happens to project onto the RMM index or by variability within the MJO itself, although it is likely to be some combination of both factors. We therefore provide conservative estimates of the variability linked to the MJO by taking the average Coh^2 between PC1 and PC2 and 250-hPa geopotential height, rather than rescaling by the factor of $\frac{1}{0.685} = 1.46$ which would provide estimates of the upper bound.

2.3.1. Statistical Significance

We use a Monte Carlo approach to estimate the bounds of statistical significance for both reanalysis and CESM2-WACCM. For the reanalysis, the lag-one autocorrelation (i.e., redness) of 250-hPa geopotential height is calculated for each grid cell across the globe for all seasons and the QBO-ignorant and easterly and westerly QBO phases. We then use the lag-one autocorrelation to generate a collection of randomly generated red noise (AR1) time series, each with the same length as the seasonal RMM time series, that is, 90 days. The mean Coh^2 of 250 bootstraps of five randomly selected instances of these red noise time series and the RMM principal component time series is then calculated. We complete this process 1,000 times, and the 95th percentile of this distribution of Coh^2 values is used as the estimate for the upper bounds of the influence of red noise on our analysis. Additional discussion regarding why we use 250 bootstraps for the observational record is within the appendix.

We also estimate the statistical significance of the difference between the Coh^2 during easterly and westerly QBO phases using a similar Monte Carlo approach. The only additional step here is that we take the difference between the mean Coh^2 of the 250 bootstrapped subsamples for the easterly and westerly QBO phases, which are generated separately using the lag-one autocorrelation for each QBO phase. We also complete this process 1,000 times and use the 2.5th and 97.5th bounds on the two-tailed distribution to estimate the significance of Coh^2 differences between QBO phases.

Table 1
Sample Sizes and Bounds of Statistical Significance for Magnitude-Squared Coherence (Coh^2)

Observational record					
Analysis separated by QBO phase					
QBO phase		DJF	MAM	JJA	SON
All	Samples		Mean of 250 bootstraps		
	$\alpha = 0.05$	0.243	0.229	0.239	0.237
Westerly	Samples		Mean of 250 bootstraps		
	$\alpha = 0.05$	0.245	0.235	0.231	0.237
Easterly	Samples		Mean of 250 bootstraps		
	$\alpha = 0.05$	0.244	0.231	0.238	0.235
Difference between westerly and easterly QBO					
QBO phase		DJF	MAM	JJA	SON
Westerly minus Easterly	Samples		10,000 realizations		
	$\alpha = .025$	3.83E-3	1.18E-3	1.41E-3	−1.77E-2
	$\alpha = .975$	9.03E-3	6.11E-3	6.66E-3	−1.18E-2
CESM2-WACCM					
Analysis separated by QBO phase					
QBO phase		DJF	MAM	JJA	SON
All	Samples		138 randomly selected		
	$\alpha = 0.05$	7.60E-3	7.64E-3	7.65E-3	7.55E-3
Westerly	Samples		138 randomly selected		
	$\alpha = 0.05$	7.70E-3	7.68E-3	7.63E-3	7.58E-3
Easterly	Samples		138 randomly selected		
	$\alpha = 0.05$	7.53E-3	7.51E-3	7.61E-3	7.46E-3
Difference between westerly and easterly QBO					
QBO Phase		DJF	MAM	JJA	SON
Westerly minus Easterly	Samples		10,000 realizations		
	$\alpha = 0.025$	−6.45E-4	−5.59E-4	−8.40E-4	−6.13E-4
	$\alpha = 0.975$	8.87E-4	8.47E-4	6.82E-4	8.23E-4

[a]All confidence bounds are calculated using a Monte Carlo approach discussed in section 2.3.1. [b]The bootstrapping method used to calculate the Coh^2 for the observational analysis is detailed in the appendices.

A slightly different approach is taken to estimate the significance bounds of the Coh^2 for CESM2-WACCM, since more samples are available, as outlined within section 2.3. Similar to the reanalysis, the lag-one autocorrelation of 250-hPa geopotential height is calculated for each grid cell across the globe for all seasons and the QBO-ignorant and easterly and westerly QBO phases. For each grid cell, the autocorrelation is then used to generate 10,000 realizations of red noise. The Coh^2 between the 10,000 red noise realizations and the RMM principal component time series, similarly split into seasons and the QBO-ignorant, westerly QBO, and easterly QBO time periods, is then calculated for each location. These bounds thereby represent the 95th percentile confidence bounds that the Coh^2 values for each season and QBO phase are distinguishable from that expected from unrelated red noise. The process for estimating the statistical significance for the differences between easterly and westerly QBO phases is similar, except we subtract the Coh^2 between the RMM time series and the red noise time series for the two QBO phases and then use the 2.5th and 97.5th percentile bounds as a two-tailed 95th percentile estimate of the significance of the difference.

After completing this process, we find that while the lag-one autocorrelation of 250-hPa geopotential height does vary across the globe with both reanalysis and CESM2-WACCM, this variability does not strongly influence the Coh^2 between the red noise realizations and RMM PC1/PC2 (Coh^2 varies less than 0.01 from the median for each season and QBO phase; data not shown). Rather, the season and QBO phase control the distribution of possible Coh^2 values between the red noise realizations and the RMM principal components

because of changes in the redness of the RMM principal component time series, and we therefore approximate the confidence bounds to depend only upon season and QBO phase and not upon latitude or longitude. The bounds selected are those from the locations of the median lag-one autocorrelation (i.e., redness) for each season and QBO phase, which are listed in Table 1.

As a result of the method we use for calculating the Coh^2 for the reanalysis data, the confidence bounds for all seasons and QBO phases are similar, even though the redness of the RMM time series varies across seasons. By averaging 250 estimates of the bootstrapped Coh^2 together, the influences of red noise are constrained to a rather narrow window. This convergence of the uncertainty permits a robust estimation of the impacts of red noise on our estimates of Coh^2 for both the raw Coh^2 values and the differences in the magnitude of Coh^2 between westerly and easterly QBO phases. For the CESM2-WACCM analysis, the number of samples used for each QBO season and phase, which is 138, is sufficiently large enough to mitigate most of the impacts of noise on the estimated Coh^2 (see appendices for more discussion). And so the bounds of statistical significance between easterly and westerly QBO phases are similarly small for CESM2-WACCM.

3. Global Teleconnection Signature of the MJO in ERA-Interim

3.1. Coherence-Based Analysis

We first determine the locations of coherent signals in 250-hPa geopotential height anomalies associated with the MJO in ERA-Interim and then calculate the mean latitudinal, hemispheric, and global distributions of such anomalies to quantify the fraction of the variance in 250-hPa geopotential height that is associated with the MJO. The subsequent analysis quantifies the dependence of the tropical and extratropical signature of the MJO on the QBO and provides a lower bound on the intraseasonal variance in 250-hPa geopotential height that is associated with the MJO.

3.1.1. QBO-Ignorant Analysis

The average Coh^2 between the two principal components of OMI and 250-hPa geopotential height anomalies across the globe is shown for all seasons for the QBO-ignorant analysis, which includes all years regardless of QBO phase, in Figure 5a. It is worth mentioning that regions of lower coherence may exhibit high coherence with the MJO within other dynamical fields. This is particularly the case for wind, given that wind anomalies are commonly in quadrature with geopotential anomalies, and so it is likely that the gaps between geopotential teleconnections are characterized by coherent MJO teleconnections in the wind field.

The extratropical signature of the MJO identified using our methods is similar to previous studies in both spatial expanse and magnitude (Alvarez et al., 2016; Henderson et al., 2016), particularly within the northern Pacific and North American regions. A Pacific-North American (PNA) teleconnection pattern-like signal is captured by the Coh^2 fields during boreal winter, with a series of maxima extending from the Indo-Pacific region throughout the northern Pacific and into North America (Figure 5a). Henderson et al. (2017) identified a similar pattern through compositing and found that this pattern results from the convective heating of the MJO over the Indo-Pacific during boreal winter. Within the Southern Hemisphere, a similar series of Coh^2 maxima extend from the Indo-Pacific region during austral winter (Figure 5c). The Southern Hemispheric signature of the MJO during austral winter has been shown to be similar to the PNA-like pattern observed within the Northern Hemisphere, with a teleconnection pattern emanating poleward and eastward from the Indo-Pacific region (Alvarez et al., 2016). Alvarez et al. (2016) showed this teleconnection pattern to be the most prominent during austral winter and spring, which is also apparent within the Coh^2-based analysis (Figures 5c and 5d).

The extratropical linkages to the MJO are most prominent during the winter of the respective hemispheres (Figures 5a and 5c). In particular, the PNA-like teleconnection pattern that emanates from the Indo-Pacific region, northward during boreal winter and southward during boreal summer, is more coherent during boreal winter than boreal summer. This increase of the winter coherence is likely associated with the more prominent circumglobal waveguide present during the winter of each hemisphere, which encourages the maintenance and propagation of extratropical circulation responses to tropical convective heating (Hoskins & Karoly, 1981; Yuan et al., 2011). Extratropical linkages do exist during hemispheric summer, although they are generally constrained to the subtropics and tend to have lower coherence than those during hemispheric winter. The extratropical signature of the MJO is markedly more scattered during fall and spring for each hemisphere, although the extratropical teleconnections during the winter and spring of each respective hemisphere do share teleconnection features (Figures 5b and 5d).

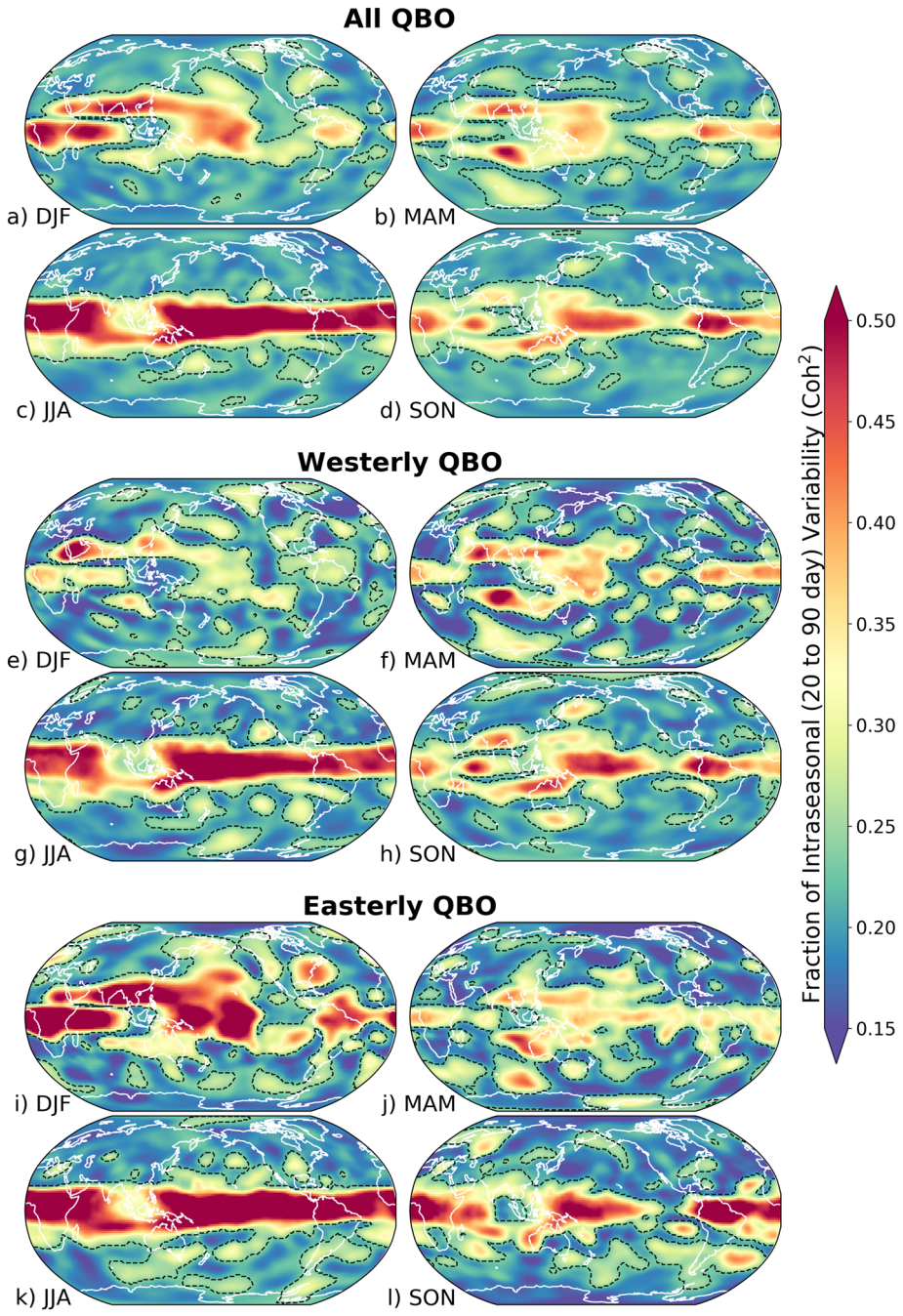

Figure 5. Magnitude-squared coherence (Coh^2) between the observational RMM index and 250-hPa geopotential height anomalies from ERA-Interim for the years 1980–2016 for the four seasons for (a–d) all periods regardless of QBO phase, (e–h) only westerly QBO phases, and (i–l) only easterly QBO phases. Regions where the Coh^2 surpasses the 95th percentile confidence bounds estimated using a Monte Carlo approach are within the dashed contours. Confidence bounds are tabulated in Table 1.

Beyond the extratropical signature of the MJO, certain features of the tropical signature differ from the expectations set forth by prior research. It is well cited in the literature that the MJO is most equatorially active during the boreal winter, with off-equatorial propagation and a generally weaker signal during boreal summer (Kiladis et al., 2014; Salby & Hendon, 1994; Wheeler & Hendon, 2004). However, according to RMM, the 250-hPa geopotential height anomalies associated with the MJO within the tropics are both substantially more coherent and zonally homogeneous during boreal summer compared to boreal winter (Figures 5a and 5c). During boreal winter, the coherence is low over the central Pacific and Atlantic oceans, which is in

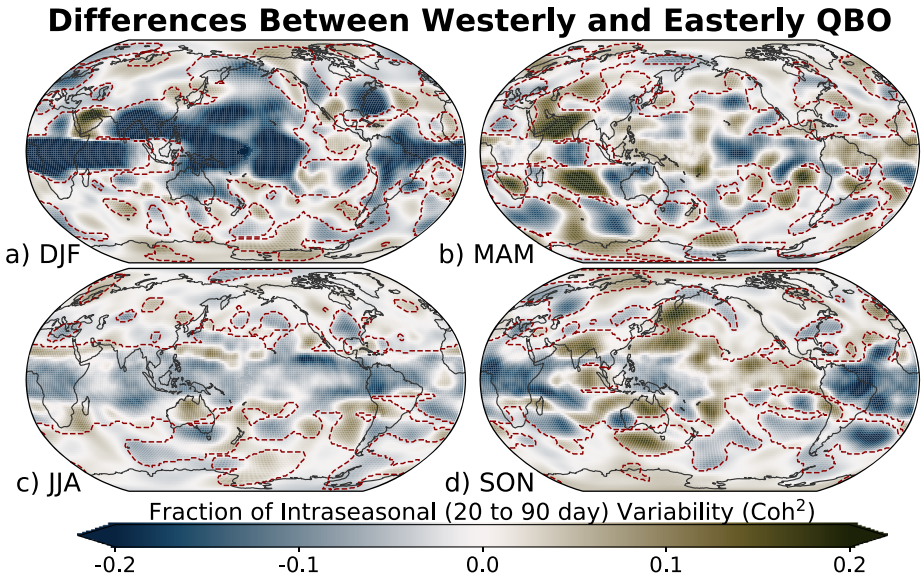

Figure 6. Difference between the Coh^2 between the observational RMM and 250-hPa geopotential height anomalies from ERA-Interim for easterly and westerly QBO phases. Positive (negative) values denote a greater Coh^2 during westerly (easterly) QBO phases. Regions where statistically significant Coh^2 values occur during either westerly or easterly QBO phases are outlined within the dashed red contour. Regions that are not statistically significant are slightly faded. Refer to section 2.3.1 for a discussion of how the significance values, which are listed in Table 1, are calculated.

stark contrast to the persistent band of high coherence across the entirety of the tropics during boreal summer. Furthermore, the amount of 250-hPa geopotential height variance within the tropics is greater during boreal summer compared to during boreal winter, which means that the increased coherence between the MJO and upper tropospheric geopotential height anomalies is also associated with an increase in the total variance of tropical 250-hPa geopotential height (further discussed in section 3.1.3).

3.1.2. QBO-Dependent Analysis

The Coh^2-based analysis is also completed for all seasons but separately for easterly and westerly QBO phases. Only seasons during which the average magnitude of zonal wind anomalies at 50-hPa is greater than 0.5σ ($\sigma = 7.27$ m s^{-1}) are considered to ensure that the QBO signal is strong (Figure 4), and all other periods, including those with strong ENSO events, are included within the analysis. The inclusion of strong ENSO periods does not change the conclusions of our study, however, and the results after removing strong ENSO periods are available within the supporting information.

Summarily, both the locations and coherence of MJO teleconnections in 250-hPa geopotential height depend on the phase of the QBO (Figure 5e through l; Figure 6). The largest differences between QBO phases occur during boreal winter, during which the coherence between the MJO and 250-hPa geopotential height anomalies is substantially magnified within the tropics during easterly QBO phases relative to westerly QBO phases (Figure 6). The locations of extratropical teleconnections of the MJO are also most different between QBO phases during boreal winter (Figure 6). The dependence of teleconnection location and coherence on QBO phase during spring and fall are less obvious, as the teleconnections are more scattered. It is interesting to note that the PNA-like teleconnection pattern of the MJO is more apparent during westerly QBO phases, although it does exist during easterly phases but with an apparent eastward shift.

The enhancement of the tropical MJO signal during boreal winter of easterly QBO phases is consistent with previous research that has shown the MJO to be more persistent and recur more frequently during easterly QBO phases (Zhang & Zhang, 2018). During boreal winter of westerly QBO phases, tropical upper tropospheric geopotential height anomalies have lesser coherence across the years (Figures 5e and 6a). Similar to the QBO-ignorant analysis, the coupling between the tropical upper troposphere and the MJO is more zonally homogeneous during boreal summer than boreal winter, regardless of QBO phase, although the coherence of the coupling during boreal summer is higher during easterly QBO phases than westerly QBO phases (Figures 5g, 5k, and 6c). A prominent gap exists in the Coh^2 within the eastern Pacific during boreal

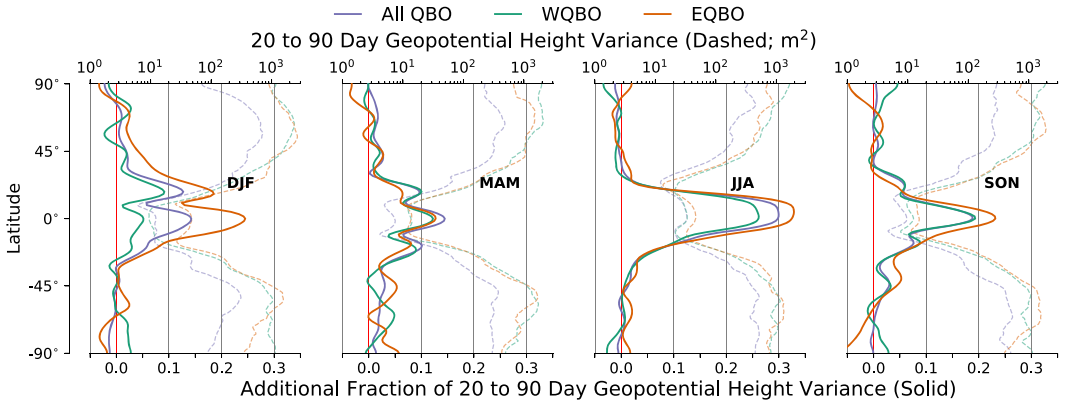

Figure 7. Longitudinal averages of (bottom abscissa; solid) the fraction of additional transient intraseasonal (20 to 90 days) variance in 250-hPa geopotential height anomalies that can be linked to the MJO based on the Coh^2 between OMI and 250-hPa geopotential anomalies (top abscissa; dashed) variance in 250-hPa geopotential height anomalies. The estimated contributions from red noise have been subtracted, and so these values represent the additional information offered from RMM beyond that which would be expected from spurious relationships between RMM and red noise within the 250-hPa geopotential height time series. The seasonal cycle is removed prior to the analysis, so these fractions include all transient modes of variability with periods ranging from 20 to 90 days. The purple line corresponds to all QBO phases and includes all years from 1980 through 2017, while the green and orange lines correspond to the westerly and easterly QBO phases respectively and only include years as detailed in Figure 4.

winter, whereas no such gap exists during the boreal summer. The presence of a secondary convective maximum during boreal summer over the eastern Pacific may drive the increased coherence within this region (Maloney & Esbensen, 2003). Another explanation may relate to the favorable conditions for extratropical waves to intrude upon the tropics within the Eastern Pacific during boreal winter due to the presence of a westerly wave duct (Webster & Holton, 1982).

The teleconnection patterns within the Pacific of each respective hemisphere during hemispheric winter are displaced between westerly and easterly QBO phases, although particularly within the northern Pacific during boreal winter (Figures 5e, 5d, 5i, 5k, 6a, and 6c). During boreal winter, geopotential height anomalies over far northwestern North America are particularly coherent during westerly QBO phases, while easterly QBO phases favor a more southward placement of the predominant teleconnection (Figure 6a). The PNA-like pattern is more prominent and shifted eastward during boreal winter of easterly QBO phases relative to westerly QBO phases, and an additional Northern Hemispheric teleconnection is perhaps apparent over eastern Russia. It is difficult to discern any pattern of the extatropical teleconnections of the MJO during spring and fall, during which the teleconnections are smaller in spatial extent and scattered across the globe (Figures 6b and 6d). The MJO undergoes a period of transition throughout spring and fall, during which the characteristics of the summer and winter MJO intermittently ebb and flow (Kikuchi et al., 2012; Kiladis et al., 2014), which may cause the more scattered teleconnection patterns during these seasons.

When the Coh^2 between 250-hPa geopotential height anomalies and the MJO is averaged across all longitudes for each QBO phase, the modulation of MJO teleconnections by the QBO becomes more apparent (Figure 7). During easterly QBO phases, the coherence of the MJO teleconnections is increased relative to westerly QBO phases within the tropics and Northern Hemispheric extratropics during boreal winter, and within the tropics during boreal summer. The tropical signature of the MJO may be suppressed during boreal spring relative to the other seasons, although the more scattered structure of the MJO teleconnections during boreal spring and fall make inference during these seasons more difficult. Within the polar regions, the Coh^2 is less than that which might be caused by spurious relationships between the RMM indices and unrelated red noise within the 250-hPa geopotential time series, and so no robust conclusions can be drawn.

It is unclear whether the shifted locations of the extratropical teleconnections between QBO phases is mainly driven by a change in the background state of the extratropical atmosphere such as a QBO-driven shift in the location of the subtropical jet (Niwano & Takahashi, 1998), or a different convective evolution of the MJO within the tropics. There are, however, observable changes to the global 250-hPa zonal wind structure

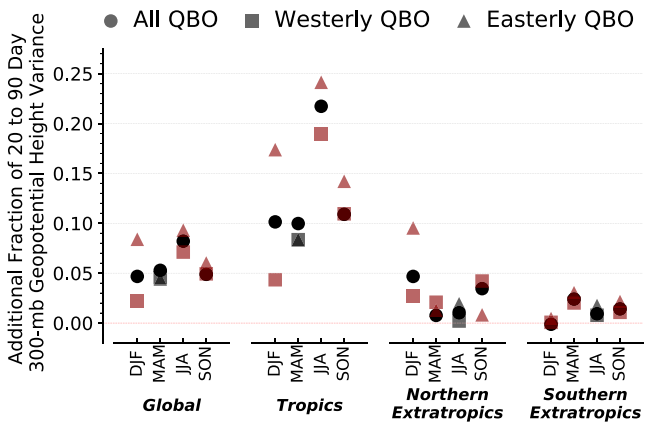

Figure 8. Fraction of additional transient, 20- to 90-day 250-hPa geopotential height variance linked to the MJO across various sub-domains of the globe, separated into season and QBO phase. The estimated contributions from red noise have been subtracted, and so these values represent the additional information offered from RMM beyond that which would be expected from spurious relationships between RMM and red noise within the 250-hPa geopotential height time series. The seasonal cycle is removed prior to the analysis, so these fractions include all transient modes of variability with periods ranging from 20 to 90 days. The following sub-domains are represented: global (left), tropics (left center; 20° S to 20° N), Northern Hemisphere extratropics (right center; 30° N to 90° N), and Southern Hemisphere extratropics (right; 30° S to 90° S). Circles represent the QBO-ignorant mean, squares the westerly QBO phases, and triangles the easterly QBO phases. Symbols colored red denote seasons and sub-domains wherein the difference between the easterly and westerly QBO phases is statistically significant at or beyond the 95th percentile according to a Monte Carlo-based test. The confidence bounds are listed in Table 1.

between QBO phases, particularly within the northern and southern Pacific (Figure S3). It is therefore reasonable to hypothesize that the modulation of MJO teleconnections by the QBO is related to changes both in the tropical structure of the MJO and the basic state of the extratropics. It has been shown by other studies that the location of the Pacific subtropical jet modulates the location of MJO teleconnections (Henderson & Maloney, 2018; Henderson et al., 2017). A similar mechanism might be responsible for the shift in the extratropical MJO teleconnections between phases of the QBO, at least within the North Pacific.

3.1.3. Hemispheric and Global Variability

We now quantify the additional fraction of hemispheric and global variability in 250-hPa geopotential height on intraseasonal timescales that is associated with the MJO, beyond that which can result from spurious relationships between red noise. To do so, the Coh^2 between PC1 and PC2 of the observational RMM and 250-hPa geopotential height anomalies is multiplied by the normalized power spectra of 250-hPa geopotential height anomalies independently for each harmonic mode, separately for each grid point and for PC1 and PC2 of RMM. Then, these quantities are summed across the 20- to 90-day band, from which the influences of red noise are subtracted. This procedure can be expressed formulaically as

$$Var_{MJO} = \sum_{T=20\ days}^{T=90\ days} (Coh^2_T)(F_{ZZ,T}) - Coh^2_{RN}, \quad (1)$$

where T denotes the period of the individual harmonic modes and F_{ZZ} is the normalized power spectrum of 250-hPa geopotential height anomalies, and Coh^2_{RN} is the 95th percentile bound of Coh^2 that results from spurious relationships between RMM and unrelated red noise within the geopotential height time series. The resultant value, Var_{MJO}, is the fraction of additional 20- to 90-day variability in 250-hPa geopotential height that can be linked to the MJO beyond what might be expected from red noise. This quantity only includes transient variability since the seasonal cycle is removed prior to the analysis.

Similar to the reasoning discussed in the last paragraphs of section 2.3, the Var_{MJO} values for PC1 and PC2 of RMM are averaged together, since each time series contains partially unique information. We subtract Coh^2_{RN} because due to a relatively small sample size within the observational record, we can only confidently discuss relative differences from noise. In doing so, we estimate the additional information the MJO provides beyond that which would result from spurious relationships between the RMM index and red noise within the 250-hPa geopotential height time series. The quantities presented therefore give a relative comparison of the coherence of teleconnections across seasons and QBO phases. Additional discussion about the influences of noise is within section 2.3 and the appendix.

Figure 8 shows the hemispheric, tropical, and global variance in 20- to 90-day 250-hPa geopotential height anomalies linked to the MJO calculated using equation (1), separated into QBO phase and season. Globally, during easterly QBO phases the MJO is associated with a greater fraction of intraseasonal variance in 250-hPa geopotential height than during boreal winter. This statement is also true for the tropics and Northern Hemispheric extratropics, wherein easterly QBO phases decidedly favor a more prominent coupling between the MJO and 250-hPa geopotential height anomalies.

During boreal winter, the QBO-ignorant analysis estimates that the fraction of 250-hPa geopotential height variance associated with the MJO is less than during easterly QBO phases and greater than during westerly QBO phases (Figure 8). Intuitively, this difference is likely caused by the combination, and therefore blending, of the easterly and westerly QBO cases into a singular analysis. *This result highlights the importance of separating MJO-related analyses that are concerned with the structure of the MJO and its teleconnections into QBO phase, since the signature of the MJO can vary substantially between easterly and westerly QBO phases.*

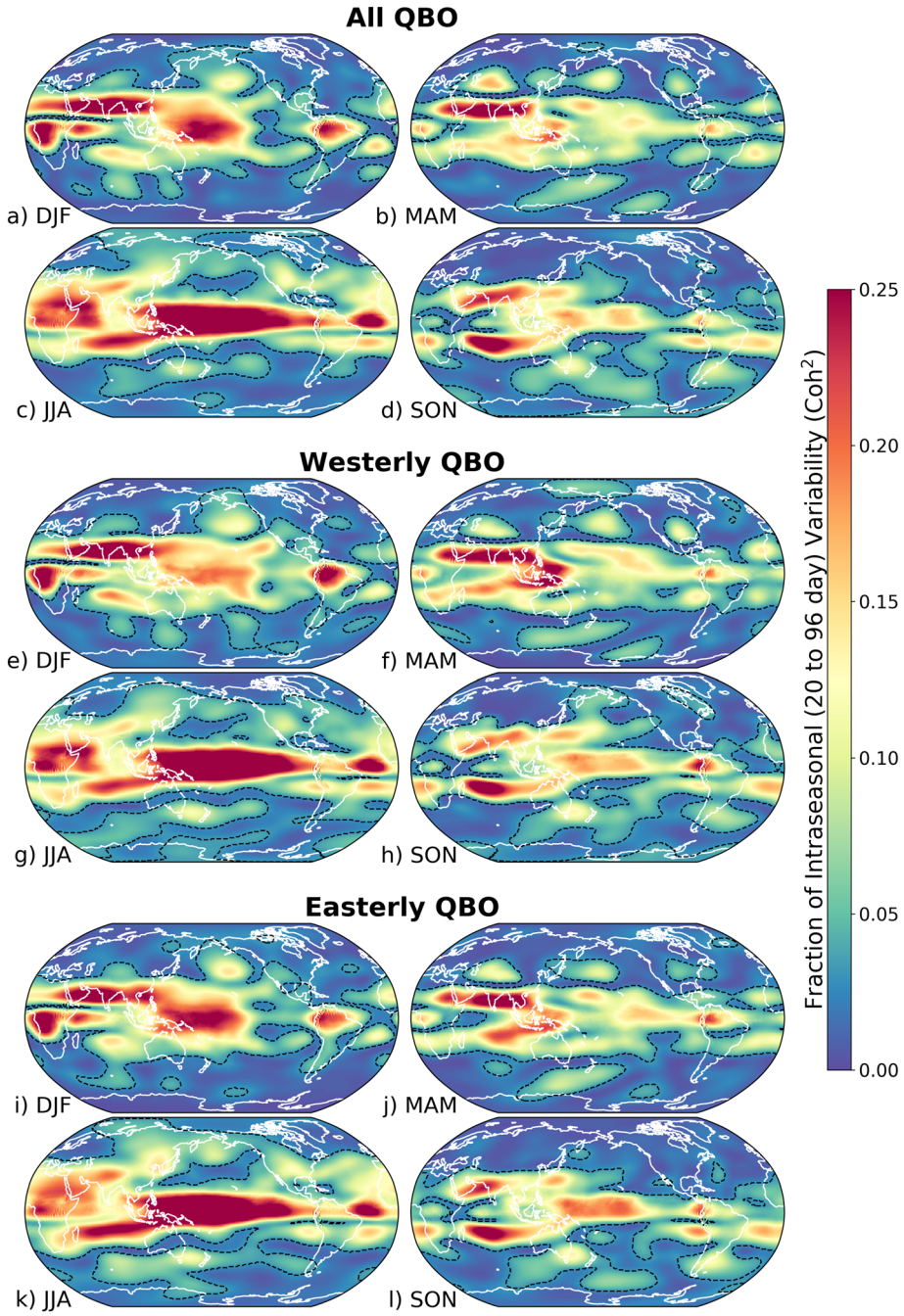

Figure 9. Magnitude-squared coherence (Coh^2) between the CESM2-WACCM RMM index and 250-hPa geopotential height anomalies from CESM2-WACCM for the four seasons for (a–d) all periods regardless of QBO phase, (e–h) only westerly QBO phases, and (i–l) only easterly QBO phases. Regions where the Coh^2 surpasses the 95th percentile confidence bounds estimated using a Monte Carlo approach are within the dashed contours. Confidence bounds are tabulated in Table 1.

It is also important to highlight that the QBO modulation of MJO teleconnections is less apparent during the spring and fall of both hemispheres, and so it is likely that this modulation does have a seasonal dependence. Furthermore, this analysis suggests that a relationship between the MJO and QBO also exists during boreal summer, particularly within the tropics.

It is interesting to note that the fraction of variance in 250-hPa geopotential height linked to the MJO does not exhibit as strong of a seasonal dependence within the Southern Hemisphere as it does within the Northern

Hemisphere. The lack of a pronounced austral winter maximum in Southern Hemispheric teleconnections may be related to either the convective maximum of the MJO being displaced north of the equator during the boreal summer (i.e., austral winter) or differences in the nature of extratropical variability between the northern and Southern Hemispheres. The proximity of the waveguides associated with the extratropical jet streams to the source of convective heating is important for the maintenance and propagation of extratropical teleconnections (Stan et al., 2017; Yuan et al., 2011). While the Southern Hemispheric jet stream moves equatorward during austral winter, the convective maximum of the MJO moves northward, away from the equator (Jiang et al., 2018). This movement of the convective maximum of the MJO to the north of the equator during austral winter may prevent the convectively generated waves from fully interacting with the austral winter waveguide.

4. Global Teleconnection Signature of the MJO Within CESM2-WACCM

The general structure of the tropical 250-hPa geopotential height anomalies associated with the MJO is similar between observations and CESM2-WACCM when QBO phase is not considered (Figures 9a–9d). For example, the magnification of the Coh^2 during boreal summer relative to boreal winter is apparent within both the reanalysis and CESM2-WACCM. During boreal winter, the Coh^2 maxima over the central Pacific and South America are similar, along with the minimum generally located over the Maritime Continent. The extratropical MJO teleconnection pattern depicted within CESM2-WACCM is different from that in observations. In particular, the Northern Hemispheric teleconnection pattern is much more prominent during boreal summer in the model than in observations. There are similarities, however, such as the presence of a Coh^2 maximum within the North Pacific for both observations and the model, along with another maximum over eastern North America during boreal spring, fall, and winter, which is indicative of the canonical Rossby wave train teleconnection pattern of the MJO.

The modulation of the 250-hPa signature of the MJO by the QBO is less apparent within CESM2-WACCM than observations, for both the tropics and extratropics (Figure 9e through l; Figure 10). In particular, the locations of the MJO teleconnections dependends less on QBO phase within CESM2-WACCM than in observations, at least within the cross-sectional plots of Coh^2 (Figure 9). With that said, there are broad similarities between the QBO modulation depicted by CESM2-WACCM and the observational record. For example, during boreal winter within both ERA-Interim and CESM2-WACCM, easterly QBO phases favor higher Coh^2 over the western tropical Pacific, and to a lesser extent within the western Indian Ocean and into equatorial Africa. CESM2-WACCM generally suggests that a modulation of MJO teleconnections by the QBO is present, particularly through differing locations in the extratropical MJO teleconnections and differences in Coh^2 magnitude within the tropics.

A statistically significant modulation does exist for most seasons within the hemispheric and global integrations of Coh^2, although the modulation is smaller within CESM2-WACCM than reanalysis (Figure 11). It is interesting to note that within the extratropics of CESM2-WACCM, the only season that does not exhibit a statistically significant difference between westerly and easterly QBO phases is boreal winter, which is the most pronounced season of QBO modulation within the observational record. It is difficult to state whether the mechanisms driving these QBO modulations are similar between ERA-Interim and CESM2-WACCM given that the teleconnection patterns are not identical between the two. However, what can be said is that the QBO does exhibit a modulation of the signature of the MJO in 250-hPa geopotential within both CESM2-WACCM and observations, although to a lesser extent within CESM2-WACCM than in observations.

5. Discussion and Conclusions

The influence of the Madden-Julian oscillation spans from the tropics to the poles. Although its influence extends across all latitudes of Earth, the location and magnitude of its impacts depend upon the background state of the atmosphere (Hendon & Abhik, 2018; Jiang et al., 2018; Slingo et al., 1999). Recent research has suggested that the tropical and extratropical character of the MJO depends on the state of the quasi-biennial oscillation (QBO), with easterly QBO phases favoring a more persistent and frequently recurring tropical convective signal of the MJO (Lee & Klingaman, 2018; Zhang & Zhang, 2018). With this in mind, we analyze the global character of upper tropospheric-lower stratospheric geopotential height anomalies connected with the MJO to determine any dependencies of these teleconnections on the state of the QBO. We also test

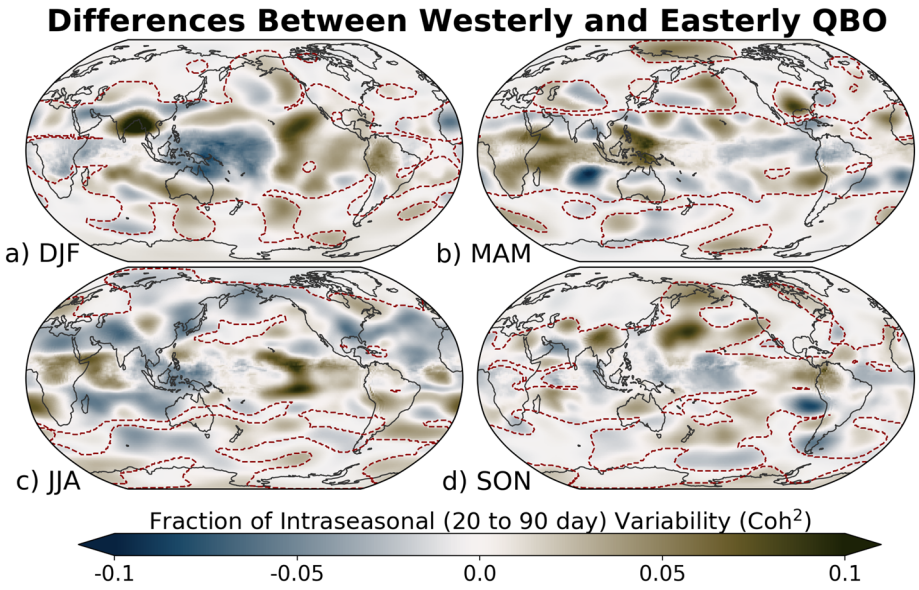

Figure 10. Difference between the Coh^2 between the CESM2-WACCM RMM and 250-hPa geopotential height anomalies from CESM2-WACCM for easterly and westerly QBO phases. Positive (negative) values denote a greater Coh^2 during westerly (easterly) QBO phases. Regions where statistically significant Coh^2 values occur during either westerly or easterly QBO phases are outlined within the dashed red contour. Regions that are not statistically significant are slightly faded. Refer to section 2.3.1 for a discussion of how the significance values, which are listed in Table 1, are calculated.

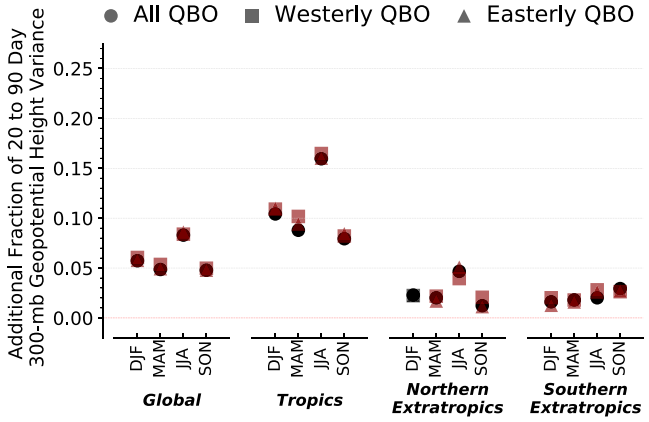

Figure 11. Fraction of additional transient, 20- to 90-day 250-hPa geopotential height variance linked to the MJO across various sub-domains of the globe within CESM2-WACCM, separated into season and QBO phase. The estimated contributions from red noise have been subtracted, and so these values represent the additional information offered from RMM beyond that which would be expected from spurious relationships between RMM and red noise within the 250-hPa geopotential height time series. The seasonal cycle is removed prior to the analysis, so these fractions include all transient modes of variability with periods ranging from 20 to 90 days. The following sub-domains are represented: global (left), tropics (left center; 20° S to 20° N), Northern Hemisphere extratropics (right center; 30° N to 90° N), and Southern Hemisphere extratropics (right; 30° S to 90° S). Circles represent the QBO-ignorant mean, squares the westerly QBO phases, and triangles the easterly QBO phases. Symbols colored red denote seasons and sub-domains wherein the difference between the easterly and westerly QBO phases is statistically significant at or beyond the 95th percentile according to a Monte Carlo-based test. The confidence bounds are listed in Table 1.

the ability of a global climate model that contains an internally generated MJO and QBO, CESM2-WACCM, to reproduce the observed modulation of MJO teleconnections by the QBO.

Within the observational record, the locations and coherence of MJO teleconnections across the globe depend on QBO phase (Figures 5–8). While easterly QBO phases favor more coherent and ubiquitous teleconnections in 250-hPa geopotential height within the tropics, the primary influence of the QBO on MJO teleconnections within the extratropics is the locations at which they occur. The modulation of QBO teleconnections is strongest during boreal winter and still exists but is less apparent during fall and spring of both hemispheres, particularly within the Southern Hemisphere where little to no modulation is found within both global integrations of Coh^2 and point-based Coh^2 anomalies. It is worth noting that our conclusions do not change when we only consider the extended summer (AMJJAS) and winter (ONDJFM) seasons, although separating the year into four seasons highlights the fact that the teleconnection patterns during spring and fall are less coherent and more scattered than those during summer and winter (Figure S5). For seasons during which the QBO modulation does exist, the coherence of MJO teleconnections for the QBO-ignorant analysis seems to be a blend of the analysis that considers each QBO phase separately. This blending is seen within both the global cross sections of Coh^2 and hemispheric and global integrations of Coh^2. It is therefore likely important to separate MJO-related analyses that are concerned with the structure of the MJO and its teleconnections into QBO phase, since the signature of the MJO can vary substantially between easterly and westerly QBO phases.

We hypothesize that the extratropical MJO-QBO relationship is related to changes in both the tropical structure of the MJO and the basic state

of the extratropics. In addition to the documented impacts of the QBO on the tropical structure of the MJO (Son et al., 2017; Zhang & Zhang, 2018), the Pacific subtropical jet and Northern Hemispheric geopotential anomalies in general are particularly sensitive to the phase of the QBO during boreal winter (Figure S3) (Boer & Hamilton, 2008). Since the strength and location of the Pacific subtropical jet has been shown to modulate the location of extratropical MJO teleconnections (Henderson & Maloney, 2018; Henderson et al., 2017), an opportunity for future research would be to separate the importance of the QBO modulation of the MJO itself and the basic state of the extratropics in dictating the locations of extratropical MJO teleconnections.

The hypothesis that the QBO modulates MJO teleconnections through both a modulation of the MJO itself and the extratropical background state is supported by comparing the boreal winter, fall, and spring teleconnections. We find that the modulation is most substantially during boreal winter, which is consistent with previous literature that has found the tropical signature of the MJO to also be maximally influenced by the QBO during this season (Son et al., 2017; Zhang & Zhang, 2018). In addition, our observational analysis suggests that the QBO modulates extratropical MJO teleconnections during the equinoctial seasons of both hemispheres, particularly within the Northern Hemisphere (Figures 6 and 8). The tropical character of the MJO is similar during November, March, and April to that during boreal winter (Kikuchi et al., 2012), and so while it could be possible that the equinoctial periods are inseparable from boreal winter for this reason, this is not the case. If it were, the sign of the influence of the QBO on MJO teleconnections would be the same during the equinoctial seasons and boreal winter, which is not observed: The impacts of the QBO on MJO teleconnections are of opposite sign during the equinoctial seasons compared to boreal winter (Figure 8).

The differences in the impacts of the QBO on MJO teleconnections across seasons therefore likely arise from more than just a modulation of the MJO itself. The modulation of teleconnections is therefore likely at least in part related to changes in the extratropical background state caused by the QBO (Figure S3) (Boer & Hamilton, 2008), given that the QBO has been found to not modulate the tropical characteristics of the MJO during the equinoctial seasons (Son et al., 2017) and yet extratropical impacts still arise. During boreal winter, the combination of the QBO impacts on the extratropical background state, and the tropical structure of the MJO may lead to the greater modulation of extratropical MJO teleconnections relative to other seasons. We leave a systematic test of these hypotheses for a future study.

The fraction of variance in 250-hPa geopotential height within the tropics that is associated with the MJO strongly depends on QBO phase during both boreal winter and boreal summer, which suggests that the coupling between the MJO and the tropical upper troposphere is sensitive to the state of the QBO during both seasons (Figure 8). The impacts of the QBO modulation of MJO teleconnections are less coherent within the extratropics during boreal summer compared to during boreal winter, however, as during boreal summer the modulation is predominantly confined to the tropics. The off-equatorial shift of the convective signal of the MJO during boreal summer may explain this seasonality. As the MJO convection shifts northward during boreal summer away from the Southern Hemispheric waveguide, it may become less likely for waves excited by the MJO convection to interact with the Southern Hemispheric jet stream compared to boreal winter, when the Northern Hemispheric jet is in closer proximity to the MJO convection.

The QBO modulation of MJO teleconnections is present within CESM2-WACCM, although it is weaker than that in observations. The modeled QBO impact manifests as a slight change in the longitudinal location of the teleconnections between QBO phases, along with higher Coh^2 within the tropical west Pacific during boreal winter of easterly QBO phases. This generally aligns with the analysis for the observational record, in that easterly QBO phases encourage greater coherence within the tropics during boreal winter. The MJO teleconnection signature within CESM2-WACCM does differ from the observational record, and so the pathways through which the QBO modulates the MJO teleconnections within CESM2-WACCM are likely different than in observations. Since the composited MJO within CESM2-WACCM is similar to the observed MJO, the differences in observed and modeled impact of the QBO on MJO teleconnections likely relate to either the weakness of the QBO in the lower stratosphere within the CMIP6 configuration of CESM2-WACCM (Figure 3) or differences in the basic state of the extratropical circulation within CESM2-WACCM and observations (e.g., Figure S3).

Another possible pathway by which the QBO may modulate MJO teleconnections is through a modulation of the polar vortex, which may subsequently impact the extratropical tropospheric circulation (Kidston

et al., 2015; Thompson et al., 2002) and thereby the development of MJO teleconnections. Two such mechanisms could involve the QBO inducing changes in the latitudinal direction of planetary wave propagation (i.e., Holton-Tan mechanism; Holton & Tan,1980) or changes in the mean meridional circulation of the stratosphere induced by the QBO which could subsequently disrupt the polar vortex through changes in planetary wave convergence within the polar stratosphere (Garfinkel et al., 2012). CESM1-WACCM has been shown to capture both of these mechanisms (Garfinkel et al., 2012); however, such a study has not yet been done for CESM2-WACCM. We leave a more thorough investigation of CESM2-WACCM's ability to simulate these various dynamical pathways for a future study.

Our study summarizes the statistics of the relationship between the QBO and the global 250-hPa geopotential height teleconnection signature of the MJO. Further investigation is needed to determine whether the modulation of MJO teleconnections by the QBO is caused by the dependence of the tropical characteristics of the MJO on the QBO or changes in the extratropical atmospheric state between QBO phases. Nevertheless, this study suggests that knowledge of the tropical stratosphere is important for understanding the coupling between the MJO and the extratropics.

Appendix A: Details of Cross-Spectral Analysis

Cross-spectra are a representation of the co-variability between the Fourier modes of two signals and therefore serve as an option for quantifying the relationship between two periodic time series. Below, we briefly introduce the mathematical formulation of cross-spectral analysis and one of its derivatives, magnitude-squared coherence.

Two time series x and y can be represented by their complex exponential Fourier expansions as

$$x(t) = \bar{x} + \frac{1}{2}\sum_{-\frac{N}{2}}^{\frac{N}{2}}(A_{xk} - iB_{xk})e^{i\left(\frac{2\pi kt}{T}\right)} = \bar{x} + \sum_{-\frac{N}{2}}^{\frac{N}{2}}F_x(k), \tag{A1}$$

$$y(t) = \bar{y} + \frac{1}{2}\sum_{-\frac{N}{2}}^{\frac{N}{2}}(A_{yk} - iB_{yk})e^{i\left(\frac{2\pi kt}{T}\right)} = \bar{y} + \sum_{-\frac{N}{2}}^{\frac{N}{2}}F_y(k), \tag{A2}$$

where A and B are the cosine and sine Fourier coefficients, t is time, T is the length of the record, $F(k)$ is the complex Fourier series as a function of wave number k, and the summation is performed across the positive and negative $\frac{N}{2}$ Fourier modes. The cross spectrum of x and y can be calculated by combining their complex Fourier series as

$$F_x(k)F_y^*(k) = \frac{1}{4}(A_{xk} - iB_{xk})e^{i\left(\frac{2\pi kt}{T}\right)}(A_{yk} - iB_{yk})e^{-i\left(\frac{2\pi kt}{T}\right)}, \tag{A3}$$

$$= \frac{1}{4}\{A_{xk}A_{yk} + B_{xk}B_{yk} + i(A_{xk}B_{yk} - A_{yk}B_{xk})\}, \tag{A4}$$

where $F_x(k)F_y^*(k)$, hereafter F_{xy}, is the complex cross spectrum and A and B are as previously defined for the Fourier expansions of x and y. Note that the complex cross spectrum can be separated into its real and imaginary parts—the real portion is the co-spectrum and the imaginary portion is the quadrature spectrum:

$$Co - spectrum = CO(k) = A_{xk}A_{yk} + B_{xk}B_{yk}, \tag{A5}$$

$$Quadrature\ spectrum = Q(k) = A_{xk}B_{yk} - A_{yk}B_{xk}. \tag{A6}$$

The co-spectrum represents the in-phase portion of x and y for each Fourier mode, while the quadrature spectrum represents the out of phase portion of x and y. Conceptually, the co-spectrum is the linear covariance between x and y as a function of wave number k. Since the complex cross spectrum is a function of wave number k, it can be segmented into bands of wave numbers and interpreted as the co-variability between x and y across a range of k. The decomposition of the complex cross spectrum can be taken a step further

to calculate the magnitude-squared coherence ($Coh^2(k)$) between the two signals. The magnitude-squared coherence between two signals is defined as

$$Coh(k)^2 = \frac{|F_{xy}(k)|^2}{F_{xx}(k)F_{yy}(k)}, \tag{A7}$$

where $|F_{xy}(k)|$ is the magnitude of the complex co-spectrum of x and y as previously defined in equation (A4) and $F_{xx}(k)$ and $F_{yy}(k)$ are their individual power spectra.

Of note, Coh^2 can be an effective metric for estimating the relationship between two periodic signals, especially if the analysis is concerned with a relationship across a specific band of wave frequencies. Previous studies (e.g., Matthews et al., 2006; Zheng et al., 2018) have used variants of linear correlation and lag compositing to extract information regarding variability related to the MJO, which are also valuable tools. Coh^2 captures the relationship between two periodic signals at specific frequency bands, which makes it a particularly useful tool for extracting information related to the MJO.

Figure A1 provides various examples of periodic signals and their associated Coh^2 and linear correlation values. Consider the case wherein the two phase-shifted signals are indeed perfectly related to one another, with one signal simply preceding the other. The relationship between the two time series perceived from linear correlation changes depending on the phase shift, whereas the Coh^2 is always unity, which more

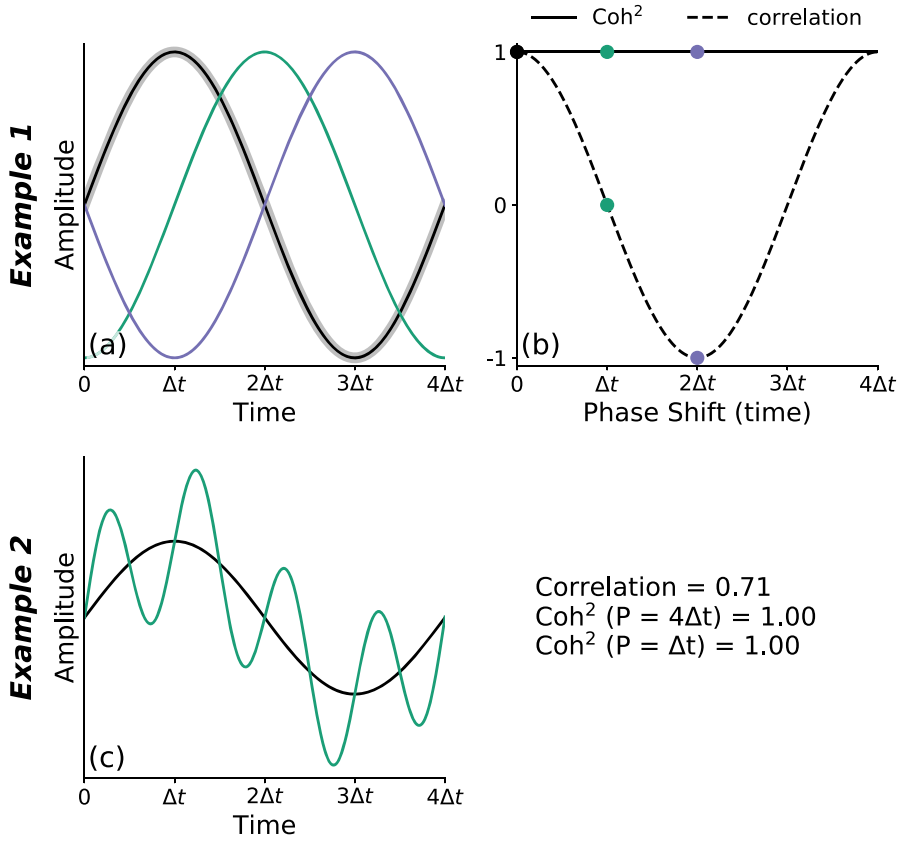

Figure A1. Example calculations of linear correlation and Coh^2 for various combinations of periodic signals. In (a) and (b), the linear correlation and Coh^2 are calculated between the base sinusoidal function (broad gray line), and the modified signals after applying a phase shift to the base function, which has a period of 4Δt. The colored dots in (b) correspond to the phase shifts of the similarly colored phase-shifted functions shown in (a). Only the Coh^2 for the P = 4Δt harmonic is shown since the sinusoids oscillate only at this periodicity. In (c), a higher frequency sinusoid (P = Δt) is added to the base sinusoid (P = 4Δt). In this case, the Coh^2 is calculated for specific wave periods to highlight the ability of Coh^2 to capture relationships at specific wave periods. The corresponding correlation and Coh^2 values between these two functions are shown to the right of panel (c). The Coh^2 for the harmonics associated with the higher frequency (P = Δt) and lower frequency (P = 4Δt) sinusoids are listed to illustrate the capabilities of Coh^2 in separating the relationships between time series with superimposed waves of different frequencies.

accurately depicts the relationship between the time series. In the most extreme case, when the phase of the waves is shifted by 90° (Δt in this example), the linear correlation decreases toward zero. Another common scenario exists through the superposition of waves, wherein the periodic signal within y that is related to x is convoluted by another coincident signal, z, with different wave characteristics than either x or y (Figure A1c). In this scenario, the linear correlation between x and y is reduced by the coincident signal z, but the Coh^2 between x and y at the period at which x oscillates is, again, unity.

These distinctions between linear correlation and Coh^2 can be important for periodic atmospheric phenomena such as teleconnections that are driven by the MJO, which are typically phase-shifted from the tropical signal of the MJO and convoluted by coincident atmospheric patterns (Henderson et al., 2017; Stan et al., 2017). In particular, since the teleconnection response to the MJO is typically realized through a propagating Rossby wave train (Henderson et al., 2017), the teleconnections of the MJO are phase shifted to different extents at different locations across the globe. The necessary lag for lag-based correlation metrics would therefore need to be calculated independently for each location, whereas for Coh^2, this phase lag is directly taken into account within the calculation.

Appendix B: Discussion of the Chosen Methods for Applying Cross-Spectral Analysis

Coh^2 can be influenced by the noisiness of a time series, in that a sufficiently large number of samples must be used to estimate Coh^2 to minimize the impacts of noise on the estimated relationship. For smaller sample sizes, as in the case of the observational record, not enough samples are available to allow a true estimation of the Coh^2 between the MJO and 250-hPa geopotential. This limitation is caused by spurious relationships between unrelated components of the two signals leading to inaccurate estimates of the true Coh^2 between the RMM index and 250-hPa geopotential anomalies. This issue presents itself in two forms. The first issue relates to the impacts of spurious relationships between noise within the two time series leading to incorrect estimations of the Coh^2. The second arises when Coh^2 values calculated for two separate time series with different numbers of samples are directly compared. Since the impacts of noise are reduced with increasing sample size, it is inappropriate to directly compare Coh^2 values for two time series with a different number of samples. It is therefore important to calculate the Coh^2 using the same number of samples for each case that is to be compared, if the Coh^2 are to be directly compared.

There are two options for mediating this problem: (1) increase the number of samples, which is not possible for the observational record, or (2) use a bootstrapping method to estimate the Coh^2, as is done here. For Method 2, a subset of the samples are selected and the Coh^2 is calculated among these subsamples, and this process is repeated many times. The idea here is that for a given number of samples, the influences of noise on Coh^2 will converge after a sufficiently large number of bootstrap instances have been completed,

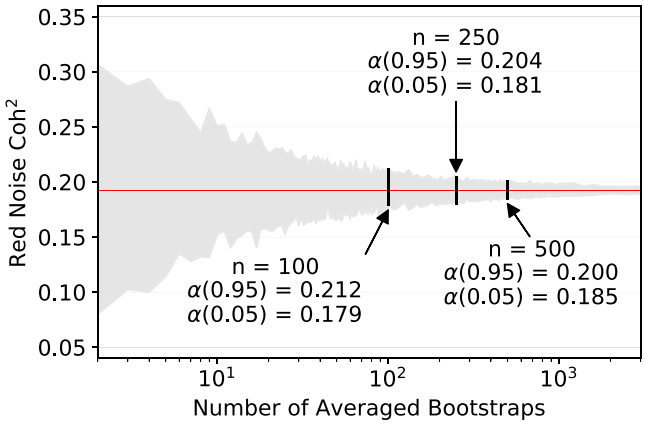

Figure B1. The 95th percentile confidence bounds on the influence of noise on estimates of Coh^2 for a red noise time series with a lag-one autocorrelation of 0.5, using five samples per individual Coh^2 estimation. The Coh^2 calculations are between randomly selected seasonal chunks of the observational RMM time series and randomly generated red noise time series of the same length.

and so the fraction of the estimated Coh^2 that is attributable to noise can be indirectly estimated. Figure B1 illustrates this concept for the case where 5 subsamples are used for each individual Coh^2 calculation, as is done for the observational analysis. It is shown that after approximately 250 bootstrapped Coh^2 calculations, the influences of noise converge upon a singular value, and the impacts of noise on the Coh^2 estimate can therefore be deduced if the redness of the 250-hPa geopotential height field is known. We therefore follow the second method for quantifying the impacts of noise on our analysis of the observational record.

In doing so, we estimate the fraction of the Coh^2 between the observational RMM record and 250-hPa geopotential anomalies that can be attributed to noise, and then we estimate deviations from this value as an indication of how much information the relationship between RMM and 250-hPa geopotential anomalies offers beyond noise. For the reanalysis, we use subsamples of five seasons for each bootstrap, with a total of 250 subsamples, and then calculate the mean of all 250 of these Coh^2 estimates. This number of subsamples is sufficient to converge the influence of spurious relationships between noise within the RMM and 250-hPa time series, which then permits the subtraction of this spurious component of the Coh^2 from the total estimated Coh^2. For CESM2-WACCM, we simply use the same number of samples for each season and QBO phase, since the impacts of noise on the estimated Coh^2 is very low for the number of samples available through the CMIP6 simulations (for our case, 138).

Acknowledgments
Benjamin A. Toms's contributions were supported by both the Office of Naval Research Grant N00014-16-1-3093 and the Department of Energy Computational Science Graduate Fellowship via Grant DE-FG02-97ER25308. Elizabeth A. Barnes's research contribution was conducted as part of the NOAA MAPP S2S Prediction Task Force and was supported by NOAA Grant NA16OAR4310064 and NOAA OWAQ Grant NA19OAR4590151. Eric D. Maloney's constributions were supported by NSF Grant AGS-1441916, NOAA MAPP Project NA15OAR4310099, and NOAA CVP Project NA18OAR4310299. Susan C. van den Heever's contributions were funded by the Office of Naval Research Grant N00014-16-1-3093. The ERA-Interim data are available from the ECMWF data server (https://www.ecmwf.int/en/forecasts/datasets/reanalysis-datasets/era-interim), and CESM2-WACCM data are available through the CMIP6 archive (https://esgf-node.llnl.gov/projects/cmip6/).

References

Adames, Á. F., Kim, D., Sobel, A. H., Del Genio, A., & Wu, J. (2017). Changes in the structure and propagation of the MJO with increasing CO2. *Journal of Advances in Modeling Earth Systems*, *9*, 1251–1268. https://doi.org/10.1002/2017MS000913

Alvarez, M. S., Vera, C. S., & Kiladis, G. N. (2017). MJO modulating the activity of the leading mode of intraseasonal variability in South America. *Atmosphere*, *8*(12), 232.

Alvarez, M. S., Vera, C. S., Kiladis, G. N., & Liebmann, B. (2016). Influence of the Madden Julian oscillation on precipitation and surface air temperature in South America. *Climate Dynamics*, *46*(1-2), 245–262.

Ashok, K., Behera, S. K., Rao, S. A., Weng, H., & Yamagata, T. (2007). El Niño Modoki and its possible teleconnection. *Journal of Geophysical Research*, *112*, C11007. https://doi.org/10.1029/2006JC003798

Baggett, C. F., Nardi, K. M., Childs, S. J., Zito, S. N., Barnes, E. A., & Maloney, E. D. (2018). Skillful subseasonal forecasts of weekly tornado and hail activity using the Madden-Julian oscillation. *Journal of Geophysical Research: Atmospheres*, *123*, 12,661–12,675. https://doi.org/10.1029/2018JD029059

Baldwin, M. P., & Dunkerton, T. J. (1998). Quasi-biennial modulation of the southern hemisphere stratospheric polar vortex. *Geophysical Research Letters*, *25*(17), 3343–3346. https://doi.org/10.1029/98GL02445

Baldwin, M. P., Gray, L. J., Dunkerton, T. J., Hamilton, K., Haynes, P. H., Randel, W. J., et al. (2001). The quasi-biennial oscillation. *Reviews of Geophysics*, *39*(2), 179–229. https://doi.org/10.1029/1999RG000073

Bessafi, M., & Wheeler, M. C. (2006). Modulation of south Indian Ocean tropical cyclones by the Madden-Julian oscillation and convectively coupled equatorial waves. *Monthly Weather Review*, *134*(2), 638–656.

Boer, G. J., & Hamilton, K. (2008). QBO influence on extratropical predictive skill. *Climate Dynamics*, *31*(7), 987–1000. https://doi.org/10.1007/s00382-008-0379-5

Charlton-Perez, A. J., Baldwin, M. P., Birner, T., Black, R. X., Butler, A. H., Calvo, N., et al. (2013). On the lack of stratospheric dynamical variability in low-top versions of the CMIP5 models. *Journal of Geophysical Research: Atmospheres*, *118*, 2494–2505. https://doi.org/10.1002/jgrd.50125

DeMott, C. A., Stan, C., & Randall, D. A. (2013). Northward propagation mechanisms of the boreal summer intraseasonal oscillation in the ERA-Interim and SP-CCSM. *Journal of Climate*, *26*(6), 1973–1992.

Dee, D. P., Uppala, S. M., Simmons, A. J., Berrisford, P., Poli, P., Kobayashi, S., et al. (2011). The ERA-Interim reanalysis: Configuration and performance of the data assimilation system. *Quarterly Journal of the Royal Meteorological Society*, *137*(656), 553–597. https://doi.org/10.1002/qj.828

Densmore, C. R., Sanabia, E. R., & Barrett, B. S. (2019). QBO influence on MJO amplitude over the Maritime Continent: Physical mechanisms and seasonality. *Monthly Weather Review*, *147*(1), 389–406.

Diaz, H. F., Hoerling, M. P., & Eischeid, J. K. (2001). ENSO variability, teleconnections and climate change. *International Journal of Climatology*, *21*(15), 1845–1862.

Eyring, V., Bony, S., Meehl, G. A., Senior, C. A., Stevens, B., Stouffer, R. J., & Taylor, K. E. (2016). Overview of the coupled model intercomparison project phase 6 (CMIP6) experimental design and organization. *Geoscientific Model Development*, *9*, 1937–1958.

Folland, C. K., Scaife, A. A., Lindesay, J., & Stephenson, D. B. (2012). How potentially predictable is northern European winter climate a season ahead? *International Journal of Climatology*, *32*(6), 801–818. https://doi.org/10.1002/joc.2314

Garfinkel, C. I., Shaw, T. A., Hartmann, D. L., & Waugh, D. W. (2012). Does the Holton–Tan mechanism explain how the quasi-biennial oscillation modulates the arctic polar vortex?. *Journal of the Atmospheric Sciences*, *69*(5), 1713–1733.

Haertel, P., Straub, K., & Budsock, A. (2015). Transforming circumnavigating kelvin waves that initiate and dissipate the Madden-Julian oscillation. *Quarterly Journal of the Royal Meteorological Society*, *141*(690), 1586–1602. https://doi.org/10.1002/qj.2461

Henderson, S. A., & Maloney, E. D. (2018). The impact of the Madden-Julian oscillation on high-latitude winter blocking during El Niño-Southern Oscillation events. *Journal of Climate*, *31*(13), 5293–5318.

Henderson, S. A., Maloney, E. D., & Barnes, E. A. (2016). The influence of the Madden-Julian oscillation on northern hemisphere winter blocking. *Journal of Climate*, *29*(12), 4597–4616. https://doi.org/10.1175/JCLI-D-15-0502.1

Henderson, S. A., Maloney, E. D., & Son, S.-W. (2017). Madden-Julian oscillation pacific teleconnections: The impact of the basic state and MJO representation in general circulation models. *Journal of Climate*, *30*(12), 4567–4587. https://doi.org/10.1175/JCLI-D-16-0789.1

Hendon, H. H., & Abhik, S. (2018). Differences in vertical structure of the Madden-Julian oscillation associated with the quasi-biennial oscillation. *Geophysical Research Letters*, *45*, 4419–4428. https://doi.org/10.1029/2018GL077207

Hendon, H. H., & Liebmann, B. (1994). Organization of convection within the Madden-Julian oscillation. *Journal of Geophysical Research*, *99*, 8073–8083. https://doi.org/10.1029/94JD00045

Holton, J. R., & Tan, H.-C. (1980). The influence of the equatorial quasi-biennial oscillation on the global circulation at 50 mb. *Journal of the Atmospheric Sciences*, *37*(10), 2200–2208.

Hoskins, B. J., & Karoly, D. J. (1981). The steady linear response of a spherical atmosphere to thermal and orographic forcing. *Journal of the Atmospheric Sciences*, *38*(6), 1179–1196.

Jiang, X., Adames, F., Zhao, M., Waliser, D., & Maloney, E. (2018). A unified moisture mode framework for seasonality of the Madden-Julian oscillation. *Journal of Climate*, *31*(11), 4215–4224. https://doi.org/10.1175/JCLI-D-17-0671.1

Jiang, X., Waliser, D. E., Olson, W. S., Tao, W.-K., L'Ecuyer, T. S., Li, K.-F., et al. (2011). Vertical diabatic heating structure of the MJO: Intercomparison between recent reanalyses and TRMM estimates. *Monthly Weather Review*, *139*(10), 3208–3223.

Kawatani, Y., Watanabe, S., Sato, K., Dunkerton, T. J., Miyahara, S., & Takahashi, M. (2010). The roles of equatorial trapped waves and internal inertia-gravity waves in driving the quasi-biennial oscillation. Part I: Zonal mean wave forcing. *Journal of the Atmospheric Sciences*, *67*(4), 963–980. https://doi.org/10.1175/2009JAS3222.1

Kemball-Cook, S. R., & Weare, B. C. (2001). The onset of convection in the Madden-Julian oscillation. *Journal of Climate*, *14*(5), 780–793. https://doi.org/10.1175/1520-0442(2001)014<0780:TOOCIT>2.0.CO;2

Kessler, W. S. (2001). EOF representations of the Madden-Julian oscillation and its connection with ENSO. *Journal of Climate*, *14*(13), 3055–3061.

Kidston, J., Scaife, A. A., Hardiman, S. C., Mitchell, D. M., Butchart, N., Baldwin, M. P., & Gray, L. J. (2015). Stratospheric influence on tropospheric jet streams, storm tracks and surface weather. *Nature Geoscience*, *8*(6), 433.

Kikuchi, K., Wang, B., & Kajikawa, Y. (2012). Bimodal representation of the tropical intraseasonal oscillation. *Climate Dynamics*, *38*(9), 1989–2000. https://doi.org/10.1007/s00382-011-1159-1

Kiladis, G. N., Dias, J., Straub, K. H., Wheeler, M. C., Tulich, S. N., Kikuchi, K., et al. (2014). A comparison of OLR and circulation-based indices for tracking the MJO. *Monthly Weather Review*, *142*(5), 1697–1715. https://doi.org/10.1175/MWR-D-13-00301.1

Kiladis, G. N., Straub, K. H., & Haertel, P. T. (2005). Zonal and vertical structure of the Madden-Julian oscillation. *Journal of the Atmospheric Sciences*, *62*(8), 2790–2809. https://doi.org/10.1175/JAS3520.1

Klotzbach, P., Abhik, S., Hendon, H., Bell, M., Lucas, C., Marshall, A., & Oliver, E. (2019). On the emerging relationship between the stratospheric quasi-biennial oscillation and the Madden-Julian oscillation. *Scientific Reports*, *9*(1), 2981.

Lauritzen, P. H., Nair, R. D., Herrington, A., Callaghan, P., Goldhaber, S., Dennis, J., et al. (2018). NCAR release of CAM-SE in CESM2. 0: A reformulation of the spectral element dynamical core in dry-mass vertical coordinates with comprehensive treatment of condensates and energy. *Journal of Advances in Modeling Earth Systems*, *10*, 1537–1570. https://doi.org/10.1029/2017MS001257

Lee, J. C. K., & Klingaman, N. P. (2018). The effect of the quasi-biennial oscillation on the Madden-Julian oscillation in the met office unified model global ocean mixed layer configuration. *Atmospheric Science Letters*, *19*(5), e816. https://doi.org/10.1002/asl.816

Lim, Y., Son, S.-W., Marshall, A. G., Hendon, H. H., & Seo, K.-H. (2019). Influence of the QBO on MJO prediction skill in the subseasonal-to-seasonal prediction models. *Climate Dynamics*, *53*, 1–15.

Lindzen, R. S., & Holton, J. R. (1968). A theory of the quasi-biennial oscillation. *Journal of the Atmospheric Sciences*, *25*(6), 1095–1107. https://doi.org/10.1175/1520-0469(1968)025<1095:ATOTQB>2.0.CO;2

Liu, H.-L., Bardeen, C. G., Foster, B. T., Lauritzen, P., Liu, J., Lu, G., et al. (2018). Development and validation of the whole atmosphere community climate model with thermosphere and ionosphere extension (WACCM-X 2.0). *Journal of Advances in Modeling Earth Systems*, *10*, 381–402. https://doi.org/10.1002/2017MS001232

Liu, S.-M., Chen, Y.-H., Rao, J., Cao, C., Li, S.-Y., Ma, M.-H., & Wang, Y.-B. (2019). Parallel comparison of major sudden stratospheric warming events in CESM1-WACCM and CESM2-WACCM. *Atmosphere*, *10*(11), 679.

Madden, R. A., & Julian, P. R. (1971). Detection of a 40–50 day oscillation in the zonal wind in the tropical pacific. *Journal of the Atmospheric Sciences*, *28*(5), 702–708.

Madden, R. A., & Julian, P. R. (1972). Description of global-scale circulation cells in the tropics with a 40–50 day period. *Journal of the Atmospheric Sciences*, *29*(6), 1109–1123.

Madden, R. A., & Julian, P. R. (1994). Observations of the 40–50-day tropical oscillation-a review. *Monthly Weather Review*, *122*(5), 814–837.

Maloney, E. D., & Esbensen, S. K. (2003). The amplification of east Pacific Madden-Julian oscillation convection and wind anomalies during June–November. *Journal of Climate*, *16*(21), 3482–3497.

Martin, Z., Wang, S., Nie, J., & Sobel, A. (2019). The impact of the qbo on mjo convection in cloud-resolving simulations. *Journal of the Atmospheric Sciences*, *76*(3), 669–688. https://doi.org/10.1175/JAS-D-18-0179.1

Matsueda, S., & Takaya, Y. (2015). The global influence of the Madden-Julian oscillation on extreme temperature events. *Journal of Climate*, *28*(10), 4141–4151.

Matthews, A. J., Hoskins, B. J., & Masutani, M. (2006). The global response to tropical heating in the Madden-Julian oscillation during the northern winter. *Quarterly Journal of the Royal Meteorological Society*, *130*(601), 1991–2011. https://doi.org/10.1256/qj.02.123

Mayer, K. J., & Barnes, E. A. (2019). Subseasonal midlatitude prediction skill following qbo-mjo activity. *Weather and Climate Dynamics Discussions*, *2019*, 1–21. https://doi.org/10.5194/wcd-2019-13

Moon, J.-Y., Wang, B., & Ha, K.-J. (2011). ENSO regulation of MJO teleconnection. *Climate Dynamics*, *37*(5-6), 1133–1149.

Mundhenk, B. D., Barnes, E. A., Maloney, E. D., & Baggett, C. F. (2018). Skillful empirical subseasonal prediction of landfalling atmospheric river activity using the Madden-Julian oscillation and quasi-biennial oscillation. *Npj Climate and Atmospheric Science*, *1*(1), 7.

Naujokat, B. (1986). An update of the observed quasi-biennial oscillation of the stratospheric winds over the tropics. *Journal of the Atmospheric Sciences*, *43*(17), 1873–1877.

Niwano, M., & Takahashi, M. (1998). The influence of the equatorial QBO on the Northern Hemisphere winter circulation of a GCM. *Journal of the Meteorological Society of Japan. Ser. II*, *76*(3), 453–461.

Pascoe, C. L., Gray, L. J., Crooks, S. A., Juckes, M. N., & Baldwin, M. P. (2005). The quasi-biennial oscillation: Analysis using ERA-40 data. *Journal of Geophysical Research*, *110*, D08105. https://doi.org/10.1029/2004JD004941

Pohl, B., Richard, Y., & Fauchereau, N. (2007). Influence of the Madden-Julian oscillation on southern African summer rainfall. *Journal of Climate*, *20*(16), 4227–4242.

Powell, S. W. (2017). Successive MJO propagation in MERRA-2 reanalysis. *Geophysical Research Letters*, *44*, 5178–5186. https://doi.org/10.1002/2017GL073399

Powell, S. W., & Houze, R. A. (2013). The cloud population and onset of the Madden-Julian oscillation over the Indian Ocean during DYNAMO-AMIE. *Journal of Geophysical Research: Atmospheres*, *118*, 11,979–11,995. https://doi.org/10.1002/2013JD020421

Richter, J. H., Butchart, N., Kawatani, Y., Bushell, A. C., Holt, L., Serva, F., et al. (2020). Response of the quasi-biennial oscillation to a warming climate in global climate models. *Quarterly Journal of the Royal Meteorological Society*. 1–29. https://doi.org/10.1002/qj.3749

Riddle, E. E., Stoner, M. B., Johnson, N. C., L'Heureux, M. L., Collins, D. C., & Feldstein, S. B. (2013). The impact of the MJO on clusters of wintertime circulation anomalies over the North American region. *Climate Dynamics*, *40*(7), 1749–1766. https://doi.org/10.1007/s00382-012-1493-y

Roundy, P. E., MacRitchie, K., Asuma, J., & Melino, T. (2010). Modulation of the global atmospheric circulation by combined activity in the Madden-Julian oscillation and the El Niño–Southern Oscillation during boreal winter. *Journal of Climate*, *23*(15), 4045–4059.

Sakaeda, N., Kiladis, G., & Dias, J. (2017). The diurnal cycle of tropical cloudiness and rainfall associated with the Madden-Julian oscillation. *Journal of Climate*, *30*(11), 3999–4020.

Salby, M. L., & Hendon, H. H. (1994). Intraseasonal behavior of clouds, temperature, and motion in the tropics. *Journal of the Atmospheric Sciences*, *51*(15), 2207–2224.

Seo, K.-H., & Lee, H.-J. (2017). Mechanisms for a PNA-like teleconnection pattern in response to the MJO. *Journal of the Atmospheric Sciences*, *74*(6), 1767–1781. https://doi.org/10.1175/JAS-D-16-0343.1

Slingo, J., Rowell, D., Sperber, K., & Nortley, F. (1999). On the predictability of the interannual behaviour of the Madden-Julian oscillation and its relationship with El Niño. *Quarterly Journal of the Royal Meteorological Society*, *125*(554), 583–609.

Son, S.-W., Lim, Y., Yoo, C., Hendon, H. H., & Kim, J. (2017). Stratospheric control of the Madden-Julian oscillation. *Journal of Climate*, *30*(6), 1909–1922. https://doi.org/10.1175/JCLI-D-16-0620.1

Stan, C., Straus, D. M., Frederiksen, J. S., Lin, H., Maloney, E. D., & Schumacher, C. (2017). Review of tropical-extratropical teleconnections on intraseasonal time scales. *Reviews of Geophysics*, *55*, 902–937. https://doi.org/10.1002/2016RG000538

Takahashi, C., & Shirooka, R. (2014). Storm track activity over the North Pacific associated with the Madden-Julian oscillation under ENSO conditions during boreal winter. *Journal of Geophysical Research: Atmospheres*, *119*, 10,663–10,683. https://doi.org/10.1002/2014JD021973

Thompson, DavidW. J., Baldwin, M. P., & Wallace, J. M. (2002). Stratospheric connection to Northern Hemisphere wintertime weather: Implications for prediction. *Journal of Climate*, *15*(12), 1421–1428. https://doi.org/10.1175/1520-0442(2002)015<1421:SCTNHW>2.0.CO;2

Trenberth, K. E. (1997). The definition of El Nino. *Bulletin of the American Meteorological Society*, *78*(12), 2771–2778.

Tseng, K.-C., Maloney, E., & Barnes, E. (2019). The consistency of MJO teleconnection patterns: An explanation using linear Rossby wave theory. *Journal of Climate*, *32*(2), 531–548.

Wang, J., Kim, H.-M., Chang, E. K. M., & Son, S.-W. (2018). Modulation of the MJO and North Pacific storm track relationship by the QBO. *Journal of Geophysical Research: Atmospheres*, *123*, 3976–3992. https://doi.org/10.1029/2017JD027977

Webster, P. J., & Holton, J. R. (1982). Cross-equatorial response to middle-latitude forcing in a zonally varying basic state. *Journal of the Atmospheric Sciences*, *39*(4), 722–733. https://doi.org/10.1175/1520-0469(1982)039<0722:CERTML>2.0.CO;2

Wheeler, M. C., & Hendon, H. H. (2004). An all-season real-time multivariate MJO index: Development of an index for monitoring and prediction. *Monthly Weather Review*, *132*(8), 1917–1932. https://doi.org/10.1175/1520-0493(2004)132<1917:AARMMI>2.0.CO;2

Wheeler, M. C., Hendon, H. H., Cleland, S., Meinke, H., & Donald, A. (2009). Impacts of the Madden-Julian oscillation on Australian rainfall and circulation. *Journal of Climate*, *22*(6), 1482–1498. https://doi.org/10.1175/2008JCLI2595.1

Yang, G.-Y., Hoskins, B., & Gray, L. (2012). The influence of the QBO on the propagation of equatorial waves into the stratosphere. *Journal of the Atmospheric Sciences*, *69*(10), 2959–2982. https://doi.org/10.1175/JAS-D-11-0342.1

Yu, J.-Y., & Kim, S. T. (2013). Identifying the types of major El Niño events since 1870. *International Journal of Climatology*, *33*(8), 2105–2112.

Yuan, J., Feldstein, S. B., Lee, S., & Tan, B. (2011). The relationship between the North Atlantic jet and tropical convection over the Indian and western Pacific Oceans. *Journal of Climate*, *24*(23), 6100–6113.

Zhang, C. (2005). Madden-Julian oscillation. *Reviews of Geophysics*, *43*, RG2003. https://doi.org/10.1029/2004RG000158

Zhang, C., & Gottschalck, J. (2002). SST anomalies of ENSO and the Madden-Julian oscillation in the equatorial Pacific. *Journal of Climate*, *15*(17), 2429–2445. https://doi.org/10.1175/1520-0442(2002)015<2429:SAOEAT>2.0.CO;2

Zhang, C., & Zhang, B. (2018). QBO-MJO connection. *Journal of Geophysical Research: Atmospheres*, *123*, 2957–2967. https://doi.org/10.1002/2017JD028171

Zheng, C., Kar-Man Chang, E., Kim, H.-M., Zhang, M., & Wang, W. (2018). Impacts of the Madden-Julian Oscillation on storm-track activity, surface air temperature, and precipitation over North America. *Journal of Climate*, *31*(15), 6113–6134.